Title

Plasticity of extrachromosomal and intrachromosomal BRAF amplifications in overcoming targeted therapy dosage challenges

Permalink

https://escholarship.org/uc/item/7qn8b3vd

Author

Song, Kai

Publication Date

2021

Supplemental Material

https://escholarship.org/uc/item/7qn8b3vd#supplemental

Peer reviewed|Thesis/dissertation

UNIVERSITY OF CALIFORNIA

Los Angeles

Plasticity of

Extrachromosomal and Intrachromosomal BRAF Amplifications

in Overcoming Targeted Therapy Dosage Challenges

A dissertation submitted in partial satisfaction of the

requirements for the degree Doctor of Philosophy

in Bioengineering

by

Kai Song

2021

ABSTRACT OF THE DISSERTATION

Plasticity of

Extrachromosomal and Intrachromosomal BRAF Amplifications

in Overcoming Targeted Therapy Dosage Challenges

by

Kai Song

Doctor of Philosophy in Bioengineering

University of California, Los Angeles, 2021

Professor Thomas Graeber, Co-Chair

Professor Daniel Kamei, Co-Chair

Focal amplifications (FAs) resulting in copy number gain of short genomic regions, can mediate targeted therapy resistance. Understanding the structure, plasticity and vulnerability of FAs is critical for designing treatments that overcome such resistance. Here we developed a combined BRAF plus MEK inhibitor resistance melanoma model that bears high mutant BRAF amplifications through two modes of FAs: extrachromosomal double minutes (ecDNA/DMs) and intrachromosomal homogenously staining regions (HSRs), and investigated FA structure and dynamics in the context of drug resistance plasticity. We found that cells harboring BRAF FAs displayed mode switching between DMs and HSRs, from both de novo genetic changes and selection of pre-existing subpopulations. Plasticity is not exclusive to ecDNAs, as cells harboring HSRs also exhibit copy number and length changes through structural loss of amplicon repeats

that allow them to respond to dose reduction and recover from drug addiction. DM and HSR mechanisms can couple with other BRAF genomic changes, such as kinase domain duplications and alternative splicing, to enhance therapy resistance. Amplicon plasticity is observed in other MAPK pathway genes, such as RAF1 and NRAS, and occurs in clinical cases of therapy resistance. We found that BRAF FA-induced dual MAPKi-resistant cells are more sensitive to pro-ferroptotic drugs, which extends the spectrum of melanoma resistance-derived ferroptosis sensitivity beyond cases of dedifferentiation.

The dissertation of Kai Song is approved.

David Nathanson

Michael Teitell

Daniel Kamei, Committee Co-Chair

Thomas Graeber, Committee Co-Chair

University of California, Los Angeles

2021

Table of Contents

List of Figures and Tables

Supplementary Table S1. M249 VSR amplicon junctions. Provided as an excel file.

Supplementary Table S2. MAPKi-treated melanoma cell lines, xenografts and patient tumors used for BRAF amplicon analysis. Provided as an excel file.

Supplementary Table S3. MAPKi-treated melanoma cell lines, xenografts and patient tumors used for BRAF amplicon analysis. Only contains pre-treatment and pos-progression pairs. Provided as an excel file.

Acknowledgments

First of and formost I would like to thank my dissertation advisor, Dr. Thomas Graeber. He is not only a knowledgeable professor with accurate foresight about the research directions, but also an optimistic mentor who always encourages me for any challenge. He helped me to brainstorm many ideas for this project, and most of them finally worked out. When I have my own thoughts, he always patiently takes them into account. It was Dr Graeber who taught me how to consider problems in unbiased ways and how to be careful about important details. I really appreciate he brought me into the realm of genomic cancer research.

Next, I want to thank all people who have significantly contributed their input to this dissertation project. They are Jenna K. Minami, Arthur Huang, Siavash Raisi, Jenschristian Luebeck, Shirley Lomeli, Gatien Moriceau, Prashanthi Dharanipragada, Oscar Krijgsman, Trevor Ridgley, Rachana Jayaraman, Asha S. Multani, Mark Goodman, William P. Crosson, Jesus Salazar, Eli Pazol, Gabriel Karin, Nikolas Balanis, Salwan Alhani, Kyle Sheu, Niroshi T. Senaratne, Kim Paraiso, Nagesh Rao, Daniel S. Peeper, Vineet Bafna and Roger S. Lo. Without their efforts or special expertise, this project would not reach to such successful stage.

Vita

Education

Nanyang Technological University (NTU), Singapore   Sep 2011 - Jul. 2015
- Bachelor of Bioengineering in School of Chemical and Biomedical Engineering
- Graduated with First Class Honors; GPA: 4.61/5.0

Research Experiences

Dissertation, graduate student researcher, University of California, Los Angeles (UCLA), USA   Jan. 2017 - now
- Lead a cancer genomics project and have shown remarkable phenotypes and identified its unique vulnerabilities
- Practice intensive experimental and computational techniques
- Mentored 6 undergrad students, 3 got accepted into PhD program, 2 went to medical school

Other experience   Apr. 2012 – now
- Was consulted by four other labs on RNAseq and gene expression chip statistical analysis, for example, for identifying key regulators in prostate cancer differentiation and upon antiandrogen treatment
- Was consulted by two other labs on single cell RNAseq data analysis
- Was consulted by a lab on running feature selection and machine learning for predicting a treatment response
- Served as a consultant for clinical survival data analysis for another lab and successfully showed glucose-6-phosphate dehydrogenase is associated with poor prognosis in breast cancer patient

Potential Publication
- Song, K., et al (2020) Plasticity of extrachromosomal and intrachromosomal BRAF amplifications in mediating targeted therapy dosage challenges. Being reviewed

Conferences
- Poster presentation, 11th Annual International Conference on Systems Biology of Human Diseases, 2018
- Speaker, SoCal Genome Stability Symposium, 2018
- Poster presentation, Friend or Foe: Transcription and RNA Meet DNA Replication and Repair, EMBL symposia, 2021
- Poster presentation, Single Cell Biology | EK26, Keystone Symposia, 2021
- Poster presentation, AACR Annual Meeting 2021

Reviewer invitations
- Cancer Research, 2019
- Proceedings of the National Academy of Sciences of the United States of America (PNAS), Assistant, 2021

Other Work Experiences

Co-president/committee member of Board of Directors, UCHA, Los Angeles, USA   Sep 2016 – Jan 2020
- handle $3 million budget each year; decide on rules and policies; preside over breach of contract hearings; address membership concerns; arbitration between member disputes

Teaching Assistant, University of California, Los Angeles (UCLA), USA   Jan. 2016 – Mar. 2016

Project Management Intern at Healthcare Sector, Siemens Pte Ltd, Singapore   Jan. 2014 - May 2014
- Installation project management; communicated with managerial board of each client; set up timelines; drafted layouts for medical equipment (e.g. CT, MRI, PET) implementation by using AutoCAD.

AIESEC swITCH Teaching Project, Dar es Salaam, Tanzania   Jun 2015 – Aug 2015
- Taught African high school students usage of several computer softwares; established network connection; designed several publicity materials to promote the school to more local students

Honors & Awards
- University BE Supplemental Fellowship, $16000+, UCLA   2017
- Presidential Scholarship, 100% stipend+tuition for 4-year study, only 2 students per department, NUS   2015
- First Class Honors degree, NTU   2015
- Outstanding Engineering Project in World Engineering Summit, top 8 team over the world, $1500   2013
- Dean's List – for students whose GPAs are in top 5%, NTU   2012
- 100% 4-year undergraduate Tuition Grant+Stipend, Ministry of Education, Singapore   2010

Chapter 1: Introduction

Genomic instability, an important enabling characteristic in cancer, confers cells with a list of aberrant hallmarks such as enhanced invasion and deregulated cellular energetics[1]. Among many types of instability-driven mutations, focal amplifications (FAs) of oncogenes in cancer genomes is a major contributor of neoplastic progression and therapeutic resistance[2–5]. There are primarily two modes of FAs: double minute (DM) and homogeneously staining region (HSR). DMs are circular extrachromosomal DNAs (ecDNAs) which allow copies of oncogenes to exist freely in nuclei and retain intact, altered or even elevated transcription activity due to high chromatin accessibility, enhancer hijacking and formation of transcription hubs[6–12]. DMs are able to replicate autonomously, but are acentric and therefore segregate into daughter cells randomly[13–16]. HSRs are intrachromosomal amplifications caused by tandem duplications of oncogene-containing regions resulting in long segments with uniform staining intensities in cytogenetics[17]. Several models regarding the generation of these two kinds of FAs have been proposed, including but not restricted to episomal, chromothripsis, breakage-fusion-bridge and integration mechanisms[18–25]. DMs and HSRs are also interchangeable via chromosomal integration and fragmentation[21,22,25–29]. The high prevalence of both kinds of FAs support their importance in tumorigenesis[15]. DMs have been observed in large number of tumors of different types, especially in neuroblastomas (31.0%) and adrenal tumors (27.6%), but rarely in normal tissues. A high occurrence of the HSR form of FAs is found in particular cancer types such as squamous cell carcinoma (12.1%) and oral cavity (10.9%), but across all cancers HSRs have a slightly lower frequency compared to DMs (0.8% vs 1.3%, respectively)[30]. FAs are present more frequently in complex neoplastic systems such as patient tumors and patient-derived cell lines (PDXs), as compared to cell lines[15].

Mutations in BRAF, a serine/threonine RAF family kinase and a key upstream member of the MAPK pathway, have been associated with many cancer types. The frequency of BRAF mutations varies widely across cancer types. For example, BRAF mutations are relatively common in thyroid gland and skin cancers (60% and 52% respectively), but are very rare in kidney cancers (0.3%)[31]. In melanoma therapy, the development of BRAF inhibitors, such as vemurafenib and dabrafenib as well as combinatorial treatments with other MAPK pathway inhibitors (MAPKi) have greatly improved patient survival[32]. However, acquired resistance often compromises the efficacy of these therapies. To date, many resistance mechanisms to BRAF inhibition emerging during clinical treatment have been identified, including reactivation of the MAPK pathway, activation of the PI3K/AKT pathway, or both. This can occur via genomic mutations, genomic rearrangements such as kinase domain duplication, altered splice isoform variant expression, cellular dedifferentiation, and other mechanisms[5,33–40]. One mechanism of reactivating the MAPK pathway that is frequently found in melanoma patient tumors is the acquisition of BRAF amplifications[5]. As previously noted, these amplifications can be mediated through both DM and HSR FA modes [36,41,42]. However, the details related to the generation, structure, dynamics, plasticities and vulnerabilities of MAPK FAs due to acquired drug resistance in melanoma are incomplete, and as such are the focus of our current study.

In this study, through acquired BRAF and MEK inhibitor resistance, we developed a melanoma model system that dynamically harbors mutant BRAF in the form of DMs, HSRs or both. Through experimentation with single-cell-derived clones, we found that increasing and/or decreasing kinase inhibitor dose is a reproducible method to modulate the number of DMs, the length of HSRs, the

transition between these FA modes, and coupling with additional genomic rearrangements such as kinase domain duplications and alternative splicing. We additionally observed plasticity of focal amplifications involving other amplified MAPK genes such as RAF1 and NRAS in additional clinically relevant driver mutation and drug combination contexts. Using optical mapping (OM) and whole genome sequencing (WGS), we profiled the BRAF FA structures and found conserved amplicon boundaries between the DM and HSR modes. Furthermore, the observed junction sequences yielded initial insight into the mechanisms of integration and HSR shortening. In investigating the cellular liabilities of BRAF amplification, we identified an increased sensitivity to ferroptosis via GPX4 inhibition, which extends the spectrum of melanoma resistance-derived ferroptosis sensitivity beyond cases of dedifferentiation. Collectively, our findings on BRAF amplicon structure, DM and HSR plasticities, and potential vulnerabilities associated with BRAF FA mediated drug resistance, highlight the challenges and provide guidance for future development of therapeutic approaches to overcome acquired MAPKi resistance in melanoma.

Chapter 2: Results

Acquired resistance to BRAF and MEK kinase inhibitors resulted in both DM and HSR karyotypes

In order to generate a FA-positive melanoma model, we treated a BRAF mutant (V600E) human melanoma cell line, M249 with the clinically used kinase inhibitor combination: vemurafenib (BRAF inhibitor, BRAFi) and selumetinib (MEK inhibitor, MEKi) to develop resistance (abbreviated as M249-VSR for vemurafenib and selumetinib resistant) as previously described[43]. The doses for both drugs were sequentially increased by roughly 2-fold, with each dose escalation taking place when cells resumed growth rates with doubling in 4 days or less. The initial and final does were 0.05µM and 2µM, respectively (Fig. 1A). Upon the establishment of cells resistant to 2µM doses, fluorescent in situ hybridization (FISH) was performed and showed a high amplification of BRAF, primarily in the DM/ecDNA form. However, over the course of a few months in culture, these cells spontaneously switched their karyotypes to DM-negative HSR-positive without any observed exceptions (Fig. 1B. See Fig. S1 and Methods section for categories and images of BRAF FA FISH-based karyotypes). To quantify the extent of FA, we performed quantitative real time PCR (qPCR) on M249-VSR-DM and -HSR cells and found that there were 30- to 40-fold increases in BRAF copy number compared to M249 parental cells which contained 5 copies of BRAF (Fig.1B and C). These amplifications also led to high protein levels of BRAF (Fig. 1D).
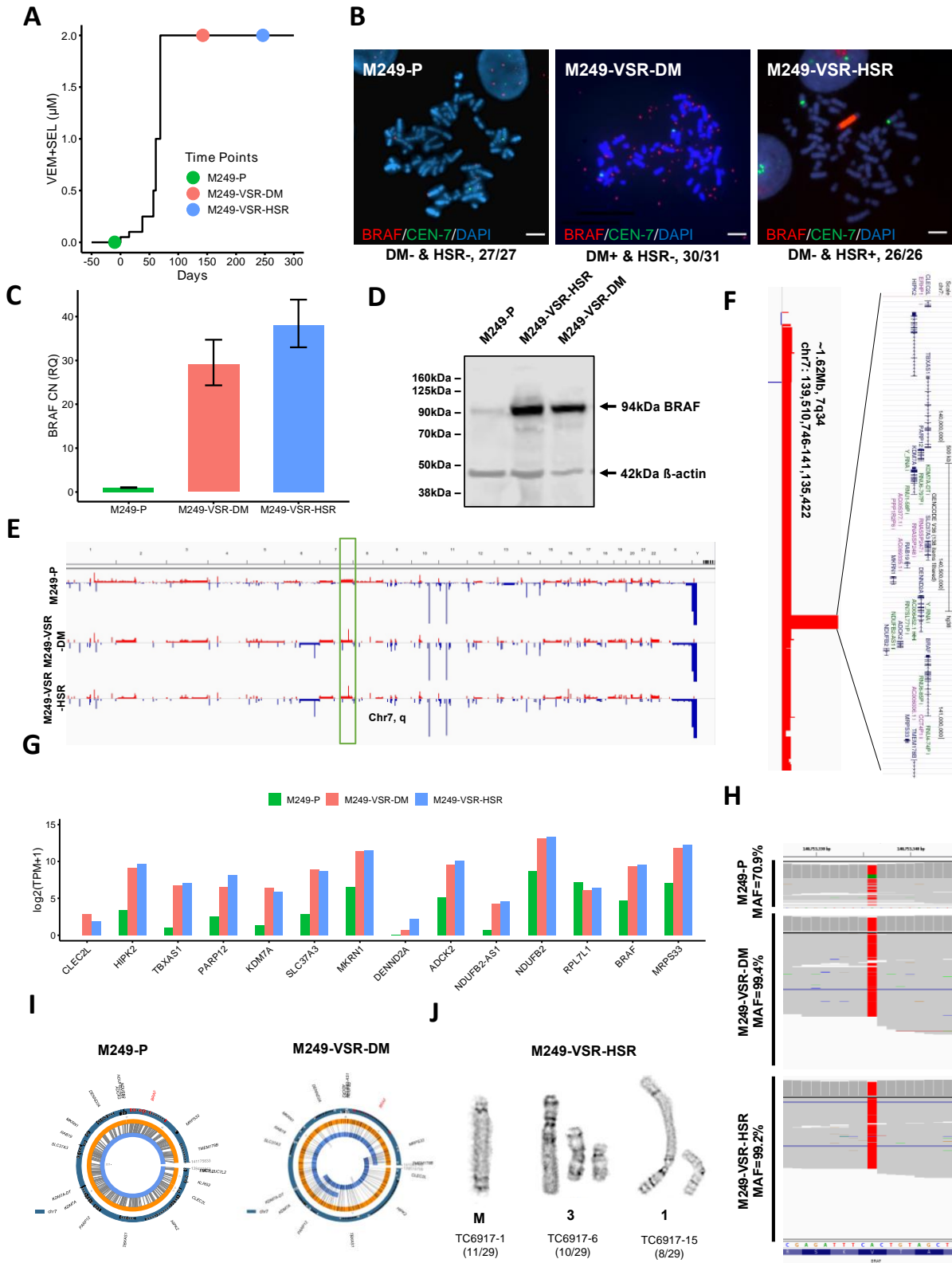
Figure 1. Focal amplifications in the form of DMs and HSRs mediate resistance to BRAF +MEK inhibition.

A, BRAFi+MEKi treatment history for M249 cells. Dots on the line represents rough sample collection points at three stages. **B**, FISH images show three different karyotypes coming from corresponding time points in (**A**) with number of observations labeled below. Red: BRAF. Green: centromere 7. Blue: DAPI. **C**, qPCR results of relative BRAF copy number in the samples from three time points in (**A**). Error bars represent t-distribution based 95% confidence intervals (see Method). CN: copy number. RQ: relative quantity. n=3. **D**, Immunoblot of BRAF for all three corresponding samples in (**A**). **E-F**, Whole genome sequencing results show that the most significant copy number increase in M249-VSR-DM and -HSR takes place at 7q34. Gene annotations within the amplicon were obtained from UCSC genome browser. **G**, mRNA level of genes that are on the amplicon of M249-VSR, measured by RNAseq. TPM: transcript per million. **H**, Frequencies of c.1799T>A (V600E) in M249-P, -VSR-DM and -VSR-HSR cells, inferred by aligning RNA-seq reads to the genome. MAF: major allele frequency. Green: thymine. Red: adenine. **I**, Bionano optical mapping results of BRAF regions in M249-P and M249-VSR-DM show the latter sample has closed circular structure for BRAF amplicon. **J**, G-banding for M249-VSR-HSR bulk cells shows HSRs are located on three different chromosomes. The frequency of each category is in parenthesis. M: marker chromosome
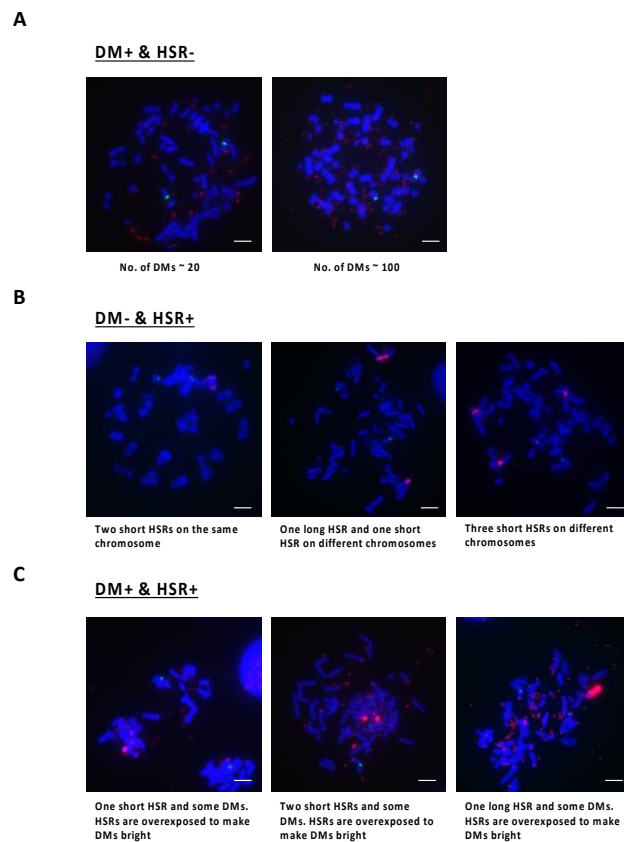
Figure S1. BRAF FA karyotype categories and subcategories.
We divided karyotypes into four primary categories: DM- & HSR-, DM+ & HSR-, DM- & HSR+, and DM+ & HSR+. Some categories have distinguishable sub-categories. Shown are representative FISH images of each BRAF FA category and sub-category. Red: BRAF. Green: centromere 7. Blue: DAPI.

Since qPCR is limited to investigating a small DNA region, we employed whole genome sequencing (WGS) and comparative genomic hybridization (CGH) for M249-P and M249-VSR cells to reveal the full copy number variations/alterations (CNV) across the genome (Fig. 1E and Supplementary Fig. S2B-C). Though there were other alterations, the most striking change upon acquisition of resistance was a FA of size ~1.62Mb at chr7q34, the region of the BRAF locus, with a fold increase consistent with qPCR results. The amplicon had highly similar start and end points in both the DM and HSR modes of amplification. Genes adjacent to BRAF on the amplicon were amplified to a similar degree (Fig. 1F); and the transcripts of these genes were also elevated as measured by RNA-seq (Fig. 1G). Such co-amplifications have also been found on amplicons containing other oncogenes, e.g. MYC and EGFR[11,12,44] RNA-seq based single nucleotide variants (SNV) calling of DM and HSR M249 cell lines indicated that the BRAF 1799T>A (V600E) mutation, the target of vemurafenib, was selected during FA development, with both DM and HSR cases displaying greater than 99% major allele frequency compared to 71% in the parental line (Fig. 1H).
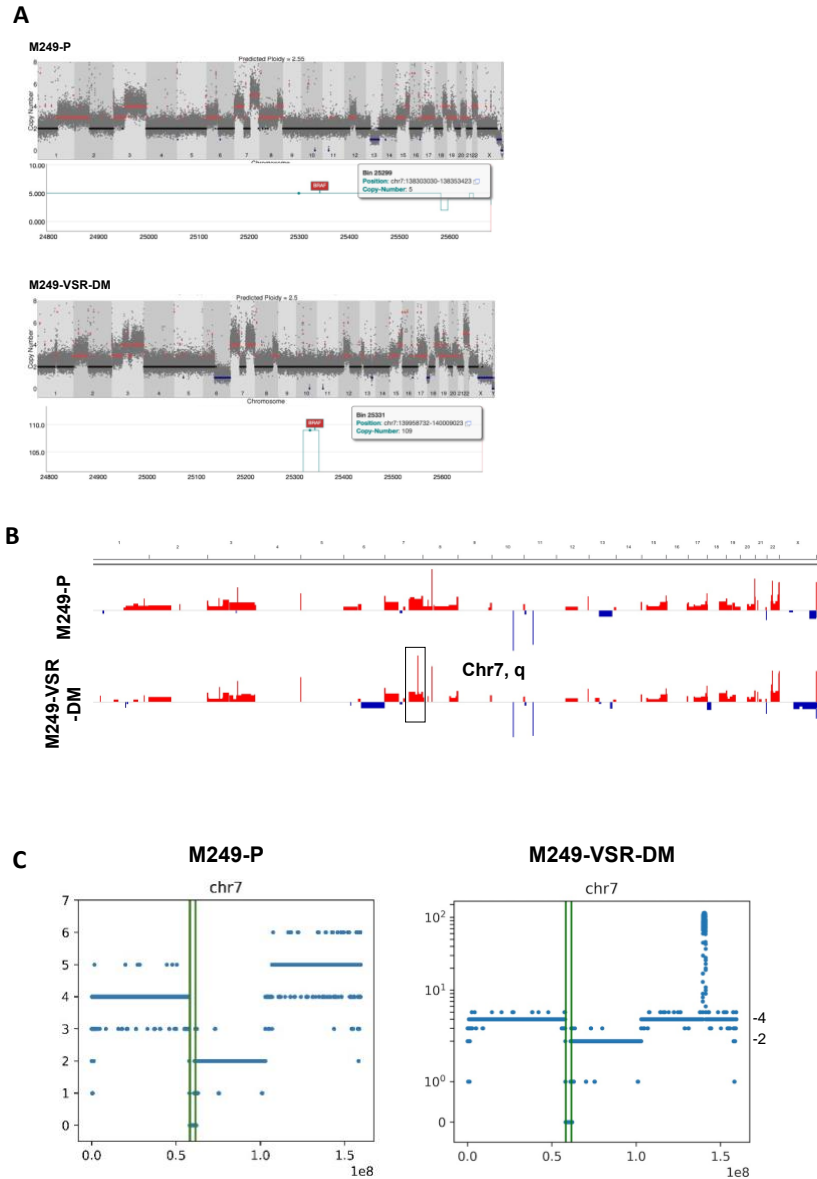
Figure S2. BRAF DNA copy number amplification results confirmed by additional methods.
Related to Fig. 1. **A,** Low-pass whole genome sequencing (WGS)-based BRAF and genome-wide copy number results of M249-P and M249-VSR-DM cells. Plotted is the whole genome CNA overview generated by the Ginkgo software. Below are the zoomed-in plots at the BRAF locus. Copy number values at the positions indicated by the green dots are shown in the inset boxes. **B**, Comparative genome hybridization (CGH) results of M249-P and M249-VSR-DM cells. The circled region highlights the BRAF focal amplicon on chromosome 7q in M249-VSR cells. **C**, Bionano optical mapping results of chr7 in M249-P and M249-VSR-DM cells. X axis: genomic coordinates. Y axis: absolute copy number.

We next characterized the structure of DM and HSR amplicons, aided by the inclusion of optical mapping (OM) data. The observed OM junctions confirmed that the DMs generated during the acquisition of resistance had a circular structure similar to common ecDNAs[6,45,46]. In contrast, the

8

parental M249 cells with 5 BRAF copies per cell show a linear arm level amplification (Fig. 1I and Fig. S2C). For HSRs, a linear and chromosomally integrated amplification mode, we investigated the sites of integration. Through cytogenetic G-banding we found a limited level of heterogeneity of HSR integration sites, with integration on either chromosome 1 or 3, or on one or more marker (unidentifiable by G-banding) chromosomes (Fig. 1J). The finding that both the DM and HSR modes contained highly similar genomic regions supports that the ensuing HSRs were generated through reintegration of DMs.

Single-cell-derived clones confirm de novo integrations of DMs into chromosomes as HSRs

To further dissect changes that occurred during the transition from DMs to HSRs, we isolated single-cell-derived clones (SCs) from the bulk M249-VSR population. These clones were isolated at an intermediary timepoint, between the DM+ & HSR- and DM- & HSR+ karyotypes (Fig. 2A). Cultures derived from these single cell clones were expanded and characterized for subsequent changes over a three-month timeframe. At the outset, three of the resultant clones had a DM+ & HSR- karyotype (SC3, SC4, and SC401), one clone had a DM- & HSR+ karyotype (SC2), and one had a DM+ & HSR+ karyotype (SC5) (Fig. 2B-C and Fig. S3). Over the matching three-month time course, the bulk population began with a small percentage of DM- & HSR+ cells which gradually expanded to dominate the population (Fig. 2B-C, B1-B4). The SCs experiments de-convoluted such changes by displaying a range of evolutionary trajectories that implicated de novo DM integration as HSRs, followed by selection of HSR+ cells.
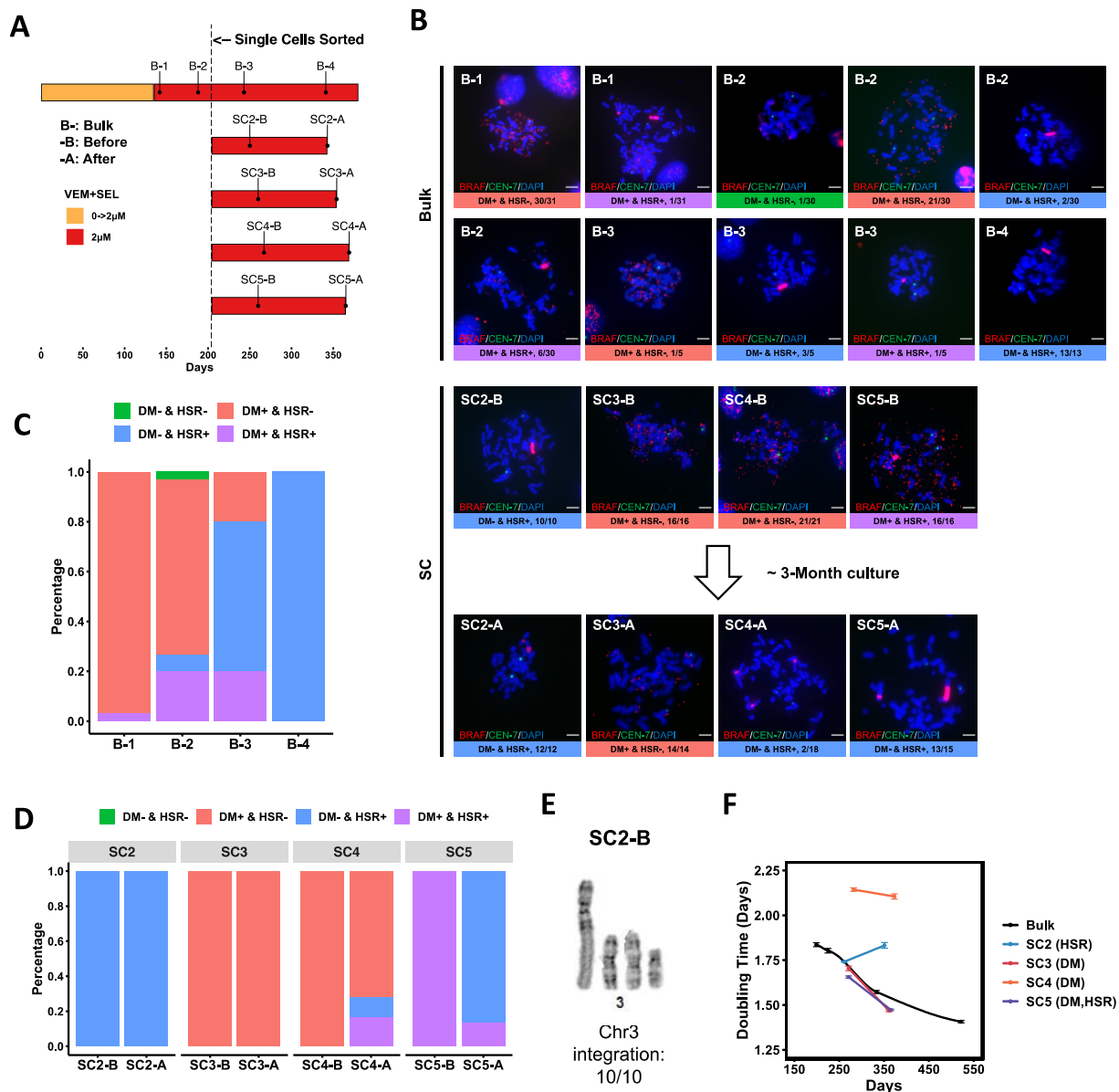
Figure 2. Single-cell-derived clones reveal de novo integrations of DMs into chromosomes as HSRs.
A, The timeline of deriving M249-VSR SCs with sampling points for FISH labeled. B-x: M249 bulk cells at different time points. SCx-B: freshly derived SCs before three-month culture. SCx-A: freshly derived SCs after three-month culture. **B**, FISH images of sampling points for both bulk and SC samples in (**A**). **C-D**, Karyotype percentages for sampling points in (**A**). **E**, The changes on doubling times for M249-VSR bulk and SC cells over time. Error bars represents standard error of means (SEMs) of doubling times, n=3 (see Method). **F**, G-banding of subclone SC2 shows HSR located on Chr3. Ratio represents the number of metaphases of such HSR chromosomal location divided by the number of all metaphases examined.
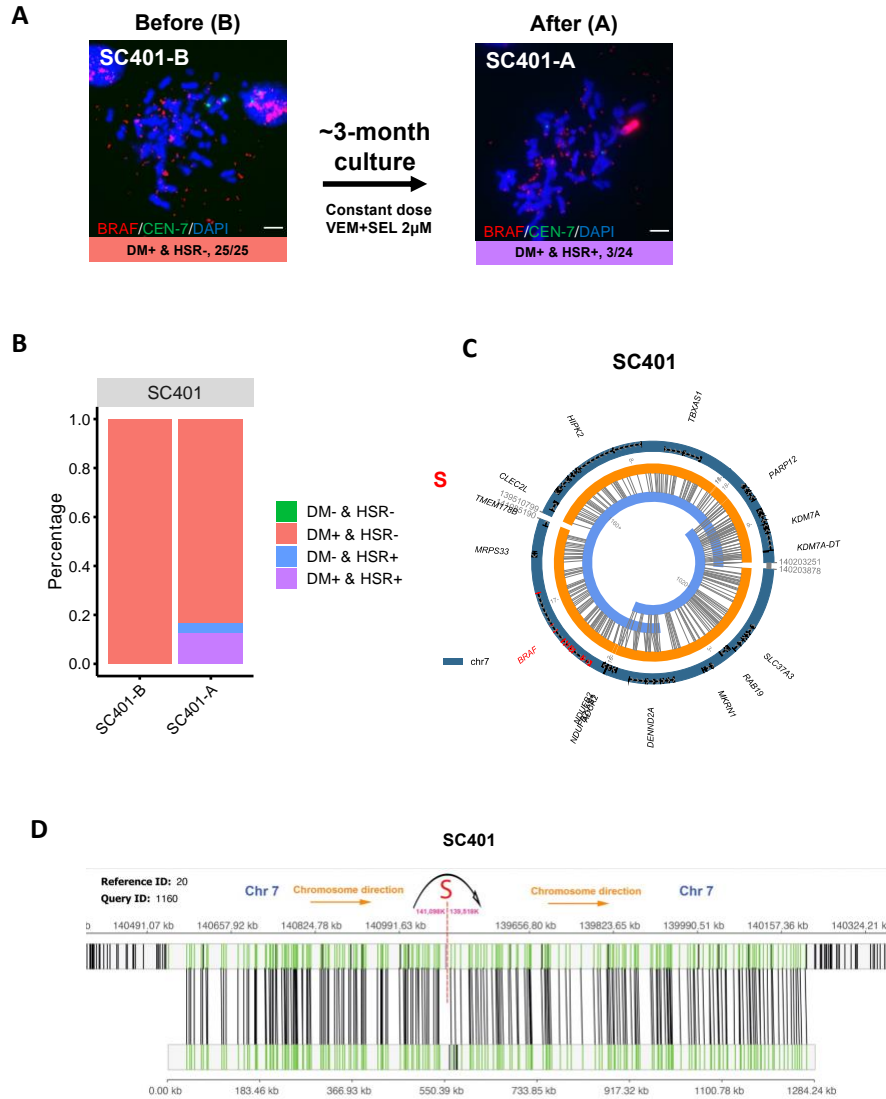
Figure S3. Single-cell-derived clone SC401 displays DM amplicon with circular structure, with subsequent chromosomal integration as an HSR.
Related to Fig 2. The SC401 clone derived from M249-VSR bulk cells was contaminated by mycoplasma during long term culture. However, it was mycoplasma negative at the time it was freshly derived. Due to this contamination, we only display data from this clone in this figure and in figure S4B. All conclusions made in the manuscript stand independent of this clone. Nevertheless, this clone remains highly consistent with the other findings, including amplicon structure and integration properties, and thus we present its data. **A-B**, Example images and karyotype frequencies of SC401 before and after 3-month culture at the constant VEM+SEL dose 2µM. -B: before. -A: after. **C-D**, BRAF circular amplicon structure in SC401 inferred by optical mapping (OM) data. S is the junction that closes the circle.

First, although the majority of SC4 cells kept their DM+ & HSR- karyotype, some cells began to

have the DM- & HSR+ karyotype and some cells harbored both DMs and HSRs (Fig. 2B and 2D).

Second, HSR+ cases of some SC4 cells presented in a format that had three smaller HSR segments

12

in different chromosomes in each cell (Fig. 2B and 2D), while only one long HSR, with or without an additional short HSR segment, was observed in M249-VSR-HSR bulk cells. Such variety of HSR arrangements demonstrates additional plasticity, either through independent de novo integration or replication and/or translocation of HSR regions. Third, a drastic FA mode switch was observed in SC5: 86.7% of the cells switched from DM+ & HSR+ to DM- & HSR+, with only 13.3% retaining the mixed karyotype (Fig. 2B and 2D). As changes occurred rapidly in SC5, cells with DM+ & HSR+ karyotypes appear to reflect an intermediate transition stage in the karyotype switch. In contrast to the initial DM+ cases, clone SC2 that only contained HSRs on chromosome 3 at the outset (Fig. 2E) maintained its karyotype for three months in culture (Fig. 2B and 2D). Finally, over the long-term culture, all subclones with DMs had their BRAF copy number decrease while the HSR BRAF copy number remained unchanged (Fig. S4A-B). The data above support that de novo integration of BRAF DMs as HSRs did occur under the steady dose of dual MAPKi treatment likely due to HSRs being a more stable mode of FA and DMs being less stable, in line with prior findings in different cell types and different treatments[21,25,27,29]. However, no changes occurred in one DM+ & HSR- clone, SC3, indicating that the tendency for integration is not absolute during the time scale observed (Fig. 2B).
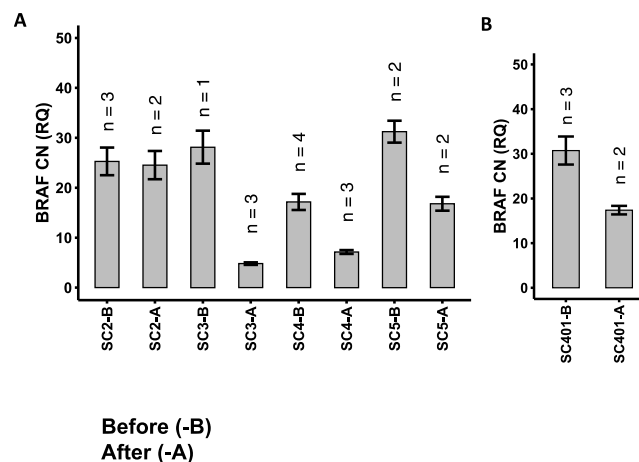
Before (-B)
After (-A)

Figure S4. BRAF amplification in DM mode decreased its copy number in single-cell-derived clones (SCs) before and after three-month culture.

13

Related to Fig 2. **A-B,** Relative quantity (RQ) of BRAF copy number (CN) before and after long term culture at constant dose, calculated by averaging multiple independent qPCR runs (n represents number of replicates). Error bars were calculated using propagation of errors.

In addition to de novo karyotype changes, we observed differences in the changes in growth rates before and after the three-month expansion among the SCs types. Two DM only (SC3, SC4) and one DM plus HSR (SC5) clones, displayed continuously increased proliferation rates (decreased doubling times) over the three-month culture. These results generally matched the increased proliferation rate seen in the bulk population. In contrast, the HSR only clone (SC2) did not increase its proliferation rate (Fig. 2D and Fig. S5A-C). In sum, these SCs-based findings demonstrate the plasticity of MAPKi-induced BRAF FAs, with a general trend of fitness-based evolution from DMs to HSRs in these conditions.
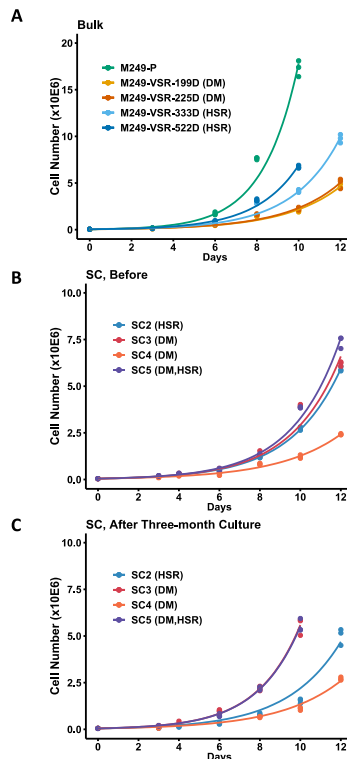
Figure S5. Bulk MAPK inhibitor resistant melanoma cells displayed an increase in growth rate over time, while SCs showed varying degrees of change in growth rate.

14

Related to Fig 2. 0.05 million cells were plated in each well of 12-well plates, and cell numbers were monitored for a maximum of 12 days. Data points were fitted to the exponential growth curve $y = y_0 \cdot e^{kx}$, where y_0 is the initial cell number, i.e. 0.05 million, y is the cell number at time x, and k is the rate constant. Three technical replicates for each time point. **A**, Bulk M249-VSR cells. The days since establishment as a resistant subculture is indicated in the legend as -xxxD. **B**, SCs shortly after single cell clone establishment. **C**, SCs after 3 months of culture.

Non-steady dose challenge can prolong or prevent DM integration into chromosomes

The observation that in the M249-VSR system DMs will integrate into chromosomes as HSRs upon continuous culture at a constant drug dose, suggests that DM+ cells have a fitness disadvantage compared to HSR+ cells in these conditions. However, DMs are often observed in tumor samples, and thus may have a fitness advantage in other situations. To test this hypothesis, we aimed to identify a scenario in which DMs would have a fitness advantage. DMs are known to segregate asymmetrically during cell division[13–16], so we tested whether an oscillating drug dose would give DM+ cells increased fitness, arguably through increased heterogeneity of the population. We designed an experiment in which we turned the double-drug doses on and off in a cycle of 8 days. DMs were indeed retained at high levels without a switch to an HSR state for a longer period of time compared to the steady dose scenario (Fig. 3A, EXP1-2). In the steady dose case, all observed cells were HSR positive on day 262, but in the oscillating dose case there was no detected HSR positive cells even approximately 7 weeks later on day 308 (Fig. 3A-3C, FIX5 and Fig. S6A-B for another DM to HSR transition control sampled earlier). However, the number of DMs did decrease in these cells (data not shown). We thus investigated whether another known MAPK inhibitor resistance mechanism had emerged in these cells. We found that these cells express the shorter BRAF splice isoform associated with acquired resistance (Fig. S6C)[35]. Hence, in response to the altered fitness challenge of a regularly changing environment, the emerging cells retained DMs longer than cells experiencing constant drug dose, and the conditions furthermore resulted in the expression of an additional resistance-associated BRAF isoform that reduced the overall BRAF expression requirement, and thus led to lower DM copy numbers.

17
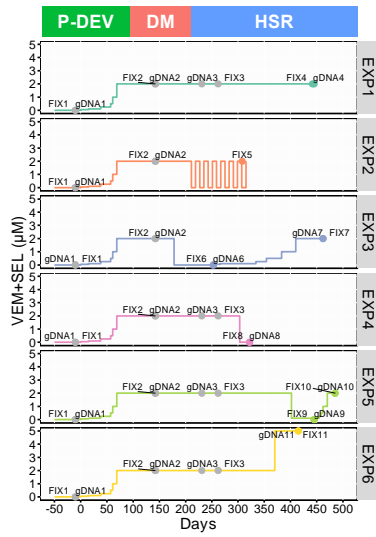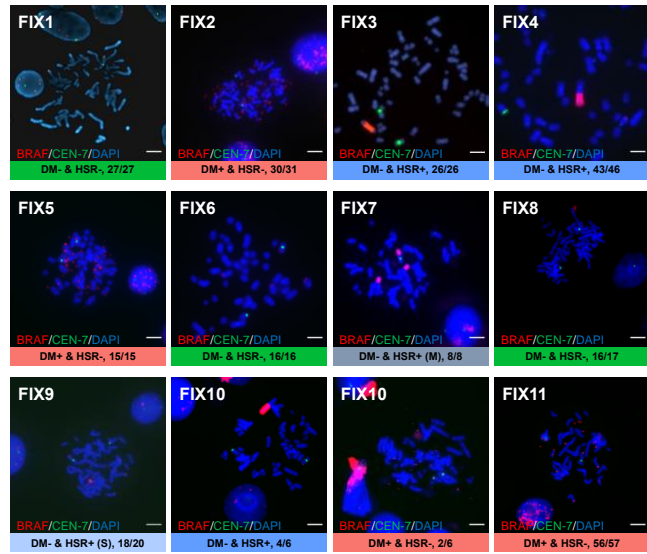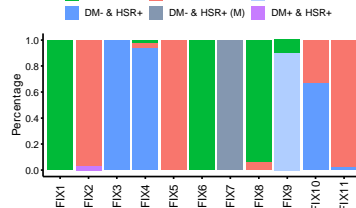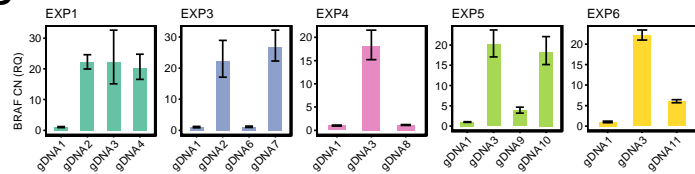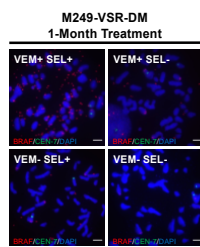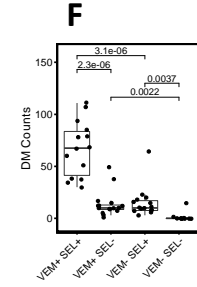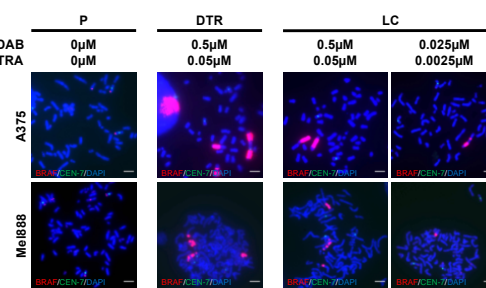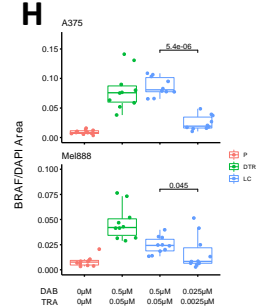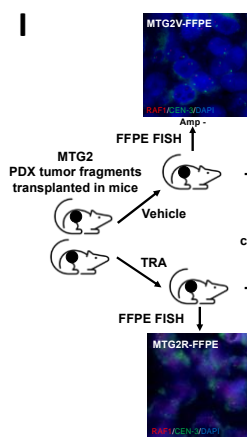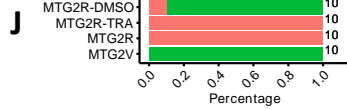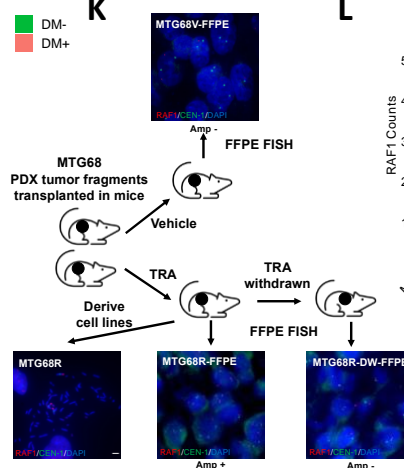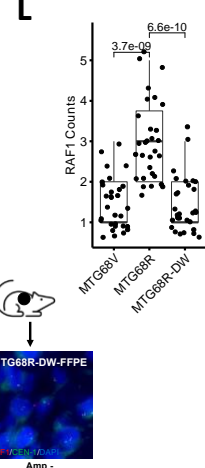
Figure 3. A variety of focal amplifications modes and secondary resistance mechanisms mediate dynamic plasticity to BRAF and MEK inhibition.

A, The treatment history of various experiments on bulk M249 VSR cells with labels of time points for when cells were fixed (FIX) for FISH and their genomic DNA (gDNA) were extracted. Top bar shows the estimated duration of each stage, inferred from Figure 2C. P-DEV: resistance developmental stage from M249 parental cells. DM: the stage when the karyotype is predominantly DM+ & HSR-. HSR: the stage when the karyotype is predominantly DM- & HSR+. Grey dots represent common time points between different experiments. **B**, Representative FISH images of fixation points in (A). Images are only shown if the corresponding karyotypes occurred at high frequencies. **C**, Full karyotype percentages of samples in (A). DM- & HSR+ (M): multiple HSRs; DM- & HSR+ (S): short HSRs. **D**, Representative qPCR results of BRAF copy number for some gDNA extraction points in (A). n=3. **E**, FISH images of M249-VSR-DM bulk cells cultured for one month with single or both drugs withdrawn. **F**, Per cell DM counts of samples in (E). P-values were calculated by two-tailed t test. **G**, FISH images of parental stage, resistance stage and the stage after a long-term culture of resistance cells at reduced dose for A375 and Mel888 cell lines. P: parental. DTR: Dabrafenib+ Trametinib resistance. LC: long-term culture. **H**, The ratios of BRAF and DAPI stain areas of samples in (G) were measured as a semi-quantification method for BRAF HSR sizes. P-values are based on one-tailed Wilcox tests. **I-L**, FFPE FISH and statistics of PDX models MTG2 and MTG68 as well as FISH and statistics of their derived cell lines for the stages after acquiring resistance to Trametinib or after drug withdrawal. PDX samples were fixed when tumor relapsed from perturbations. Number of metaphases analyzed are labeled on the right side of the bars in (J). P values in (L) were calculated using two-tailed t test. TRA: Trametinib. V: vehicle. R: resistance. DW: drug withdrawal. Amp: amplification

18
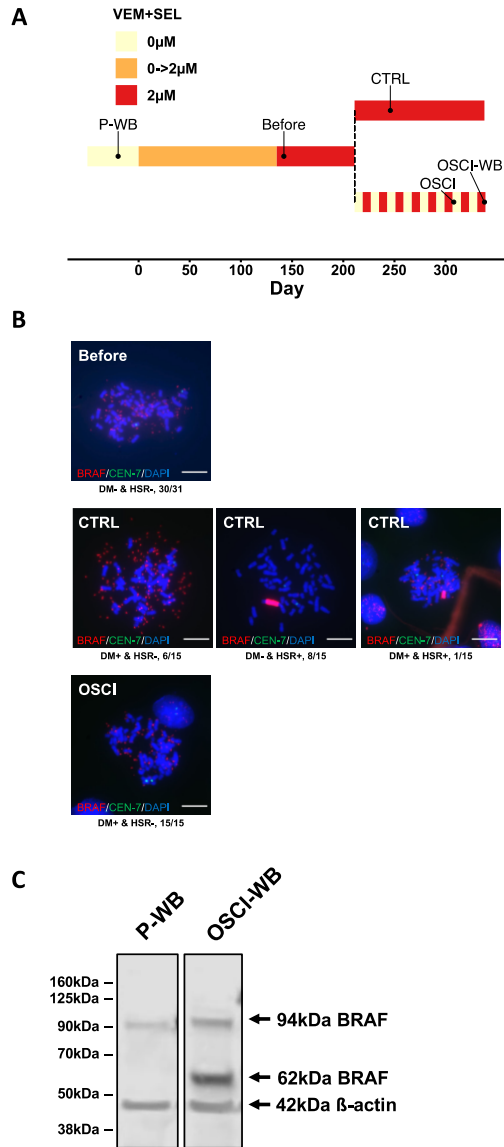
Figure S6. Treating DM+ cells with oscillating doses of BRAF and MEK inhibitors conferred a selection advantage for the DM+ & HSR- subpopulation.
Related to Fig 3. **A**, Oscillating (OSCI) and steady dose (CTRL) treatment schemes of M249-VSR-DM cells using VEM+SEL. **B**, Representative FISH images for the sampling points indicated in (**A**). **C**, Western blot results for M249 Parental sample and M249-VSR with oscillating dose (labeled in **A**).

19

MAPKi-induced DMs and HSRs display dynamic plasticity upon changes in drug dose

Next, we focused on studying the plasticity of DMs and HSRs in M249-VSR cells. As a foundation for this analysis, we first examined whether HSRs were the final stable form of amplicons for cells kept under constant drug dose by checking their karyotypes after a few additional months. We found that most cells still harbored HSRs with similar amplicon length and BRAF copy number (Fig. 3A-D, EXP1). This stable result provides our reference control for comparison to other cases with drug dose manipulation.

To evaluate if the DM to HSR trajectory observed under constant inhibitor dose could be affected by changes in dosing, we next either decreased or elevated the double-drug concentration being applied to DM+ or HSR+ cells. Previous studies have examined the potential of using drug holidays to eliminate drug-addicted cells[39,42,43,47], thus sparking our interest in studying the effect of this approach on DMs and HSRs. To investigate this, we withdrew VEM+SEL treatment from M249-VSR-DM and -HSR cells. In the DM+ case, when doses were acutely brought down from 2µM to 0µM, all DMs were eliminated based on FISH analysis with the fastest change observed in 12 days. qPCR results showed that the copy number of BRAF was reduced drastically (Fig. 3A-D, EXP3; Fig. S7A-C). We also performed experiments in which only one of the two drugs was withdrawn. Upon single drug withdrawal we saw reduction in DM copy number in as little as 1 month (Fig. 3E-F), but in notable contrast to the double drug removal there were minimal effects on cell viability and growth rates (Fig. S8A-B).
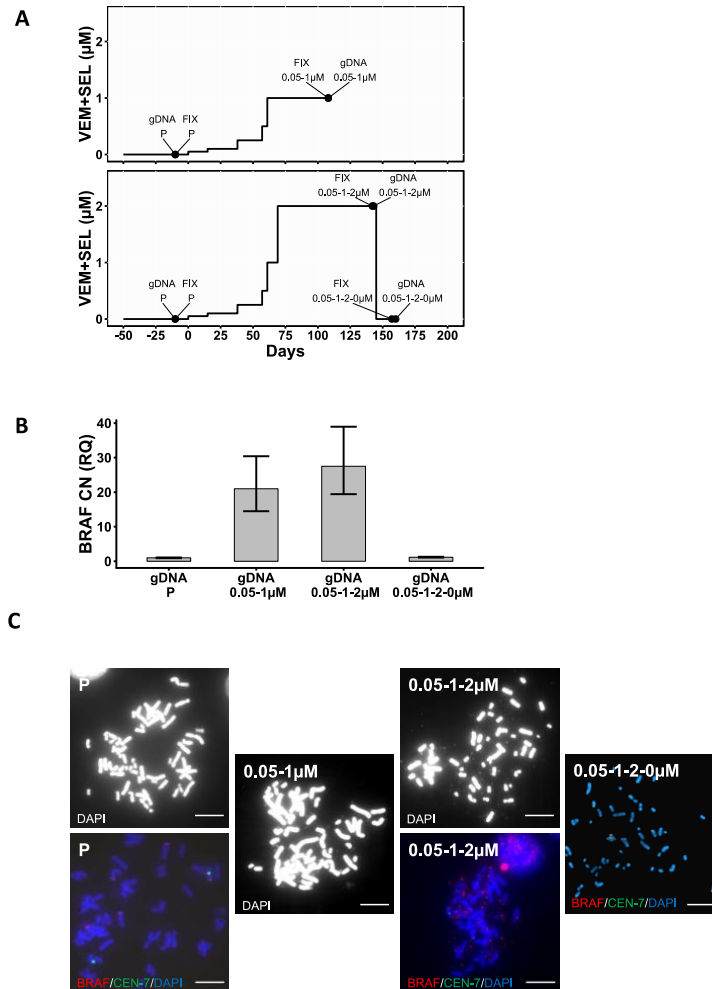
Figure S7. Double drug withdrawal eliminated BRAF-carrying DMs in about 15 days.
Related to Fig 3. **A**, Treatment scheme of M249 cells with VEM+SEL. Points shown represent when cells were fixed (FIX) and collected for genomic DNA (gDNA). **B**, qPCR results of relative BRAF copy number for the time points in (**A**). CN: copy number. RQ: relative quantity. **C**, Representative metaphase spread images and FISH images for the time points in (**A**).

A prompt reversion of BRAF copy number to the parental state in three weeks also occurred in HSR cells upon full removal of the dual inhibitors (Fig. 3A-D, EXP4). Notably, there was not a substantial difference between the recovery time of DM and HSR cells in these drug wash-out experiments (Fig. S8A-B). These results motivated additional experiments to test the plasticity of the HSR FA mode. We next repeated the dose decrease experiment above using the bulk population in its HSR+ state but did not perform a complete withdrawal (Fig. 3A-C, EXP5: 2µM to 0.1µM). In this experiment, the bulk population demonstrated a substantial shortening of the

typical HSR length, but HSRs were still detectable. Using this new sub-population, we further explored the cellular genomic plasticity by subsequently reinstating the 2μM double drug dose. The cells regained resistance in less than a month, and most cells again presented with the longer form of HSRs (Fig. 3A-C, EXP5). During the interval of drug reduction and increase, BRAF DNA copy number also decreased following the 2μM to 0.1μM transition, and re-increased following the 0.1μM to 2μM transition accordingly (Fig. 3D, EXP5).
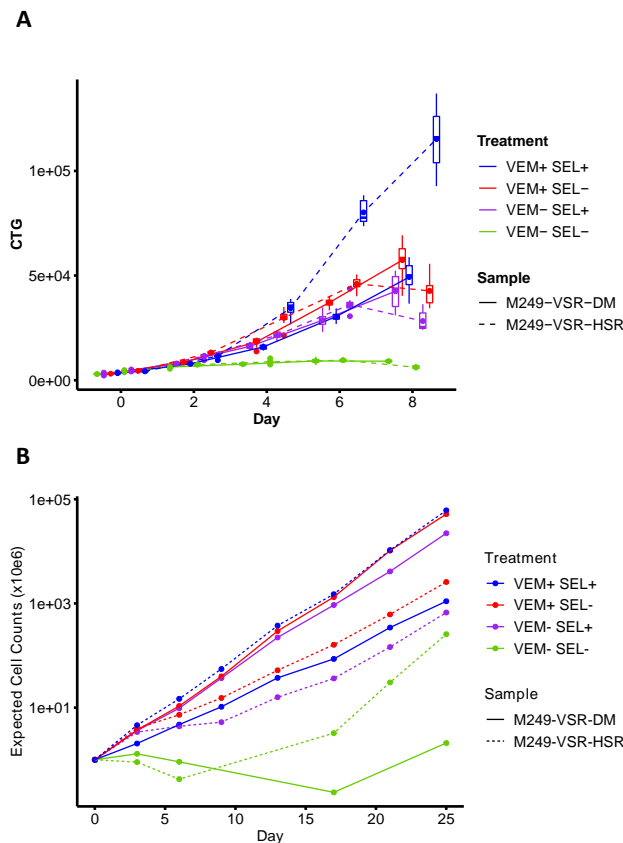
Figure S8. DM+ M249-VSR cells tolerate single-drug withdrawal better than HSR+ cells, but there is no difference on recovery rate between DM and HSR cells for double-drug withdrawal.
Related to Fig. 3. **A**, Short term viability and growth rates for M249-VSR-DM and HSR bulk cells upon acute withdraw of one of or both MAPK inhibitors. Viability was measured by the CellTiter-Glo (CTG) Luminescent assay. **B**, Long term growth rate measurement for the same treatments in (**A**). Expected cells counts were calculated by multiplying all cell number fold changes (measured upon each passage) together.

We also reinstated a 2μM drug dose on the bulk population of cells that had drug withdrawal (0μM) occur while they were in the DM+ state (Fig. 3A, EXP3). In this case, it took about 4 months for

the cells to re-develop resistance to VEM+SEL, similar to the time required for the initial establishment of resistance in the parental cells. In this experiment, the melanoma cells demonstrated an additional variation in that upon becoming resistant they typically harbored three separate shorter HSRs on different chromosomes (Fig. 3B-C, EXP3). None of the cells presented with a single larger HSR. This treatment course thus further revealed the plasticity of genomic options available for adjusting to changes in selection pressures.

Notably, we could generalize a subset of these copy number plasticity findings to other melanoma samples and other amplified genes under MAPKi challenge. Cell lines A375 and Mel888 harbor BRAF HSRs upon acquiring Dabrafenib (BRAFi) plus Trametinib (MEKi) resistance (DTR) and harbor shortened HSRs after dose reduction (Fig. 3G-H). In an additional example, we found the copy number of RAF1 (CRAF), a protein that forms heterodimers with BRAF for ERK activation[48,49], can also mediate Trametinib (MEKi, abbreviated as TRA) adaption. RAF1 amplifications existed in both extra- and intra-chromosomal modes in patient-derived xenograft (PDX) tumors resistant to TRA and disappeared after drug withdrawal (Fig. 3I-L). To our knowledge, this is the first report on RAF1 amplification, as opposed to RAF1 elevation through post-transcriptional mechanisms[50], mediating MAPKi resistance.

Single-cell-derived clones demonstrate a de novo component to the plasticity of BRAF DM and HSR focal amplifications

The dose decrease and increase results above could be explained by selection for residual BRAF copy number-low or -high cells in the respective populations. To investigate cellular plasticity to dramatic drug reduction in a more homogeneous population, we turned to the single cell-derived DM+ or HSR+ clones. In these experiments we lowered the VEM+SEL double dose from 2µM to 0.1µM using clones SC2 (HSR), SC302 (HSR), SC3 (DM) and SC4 (DM). In the post-drug-decrease populations, SC2 and SC302 showed reduced length of HSRs, and SC3 and SC4 showed reduced number of DMs. All cases were accompanied by a substantial decrease in BRAF copy number (Fig. 4A-C, Fig. S9A-C). Another characteristic that indicates the plasticity of HSR-harboring cells is comparable to that of the DM case is that the recovery times upon dose withdrawal for DM+ or HSR+ cells, either bulk or as SCs, were not substantially different (Fig. 4D).
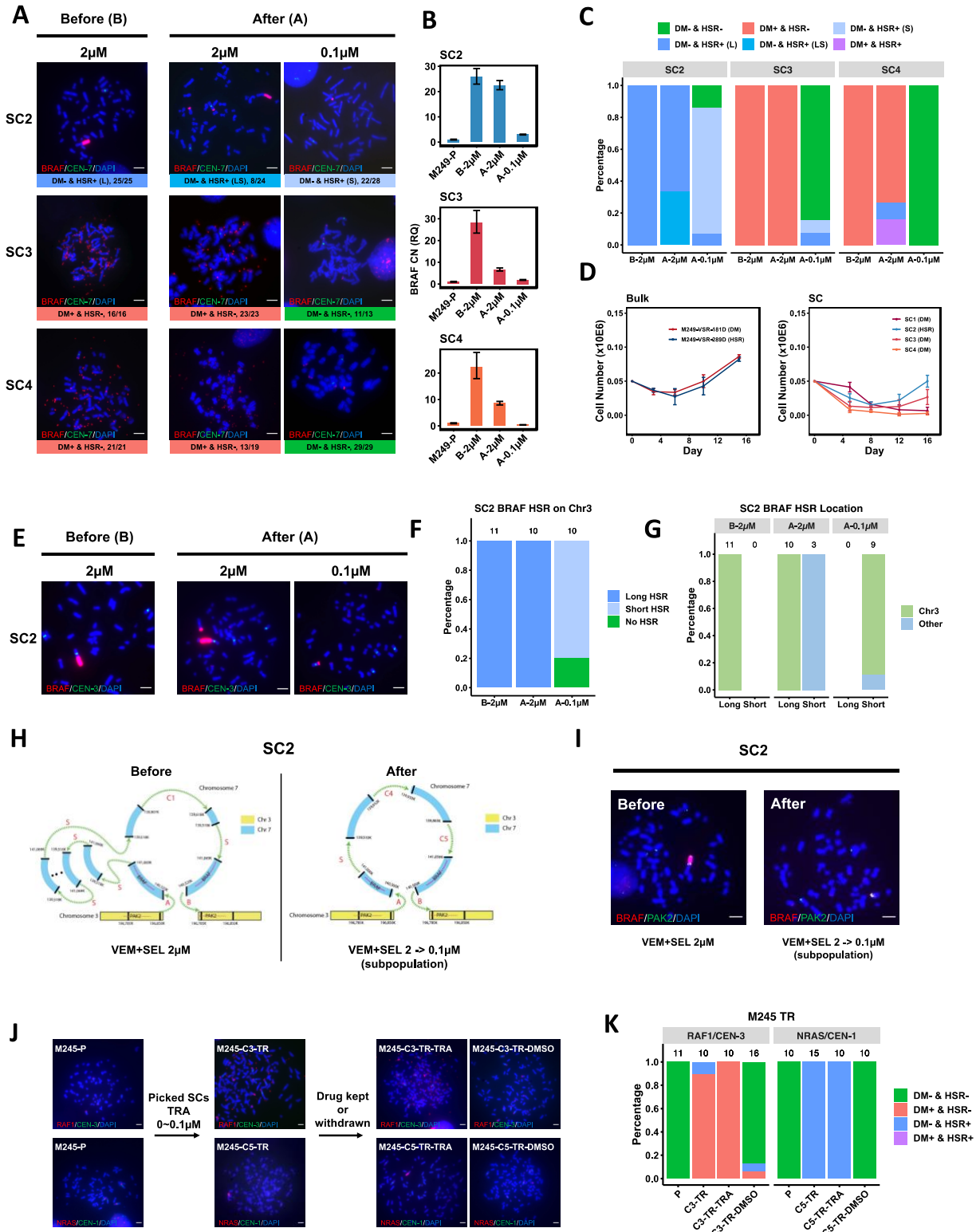
Figure 4. The plasticity of BRAF amplification is reproducible at single cell level, supporting de novo genomic changes in addition to selection.

A, Representative FISH images of three SCs that were treated either with 2µM (original dose) or 0.1µM VEM+SEL for roughly three months. LS: long and short HSR in one cell. L: long HSR. S: short HSR. **B**, qPCR of samples in (**A**). n=3. B-: before three-month culture. A-: after three-month culture. **C**, The full percentage of each karyotype for samples in (**A**). **D**, Cell number measurements after VEM+SEL was withdrawn from M249-VSR bulk cells and SCs. Error bars are standard deviations from three technical replicates. Predominant BRAF FA modes are denoted in parenthesis. **E**. RAF1 or NRAS FISH images of two M245 SCs upon becoming resistance to Trametinib and recovered from Trametinib withdrawal. P: parental. TRA: Trametinib. TR: Trametinib resistance. **F**. Frequencies of karyotypes for samples in (**E**). Number of metaphases analyzed are on the top of the bars. **G**. FISH images of M249 SC2 before and after VEM+SEL dose reduced from 2µM to 0.1µM or kept at 2µM using BRAF and chromosome 3 centromere probes. **H**, A summary of what kind of HSR is on chromosome 3 in each cell before and after VEM+SEL dose reduction in (**G**). Number of metaphases analyzed are on top of the bars. **I**, A summary of whether long and short HSRs are on chromosome 3 or other chromosomes before and after VEM+SEL dose reduction in (**G**). **J,** BRAF HSR integration structure inferred by optical mapping data before and after VEM+SEL dose reduction. **K**, FISH images with BRAF and PAK2 probes supporting the structure in (**J**).
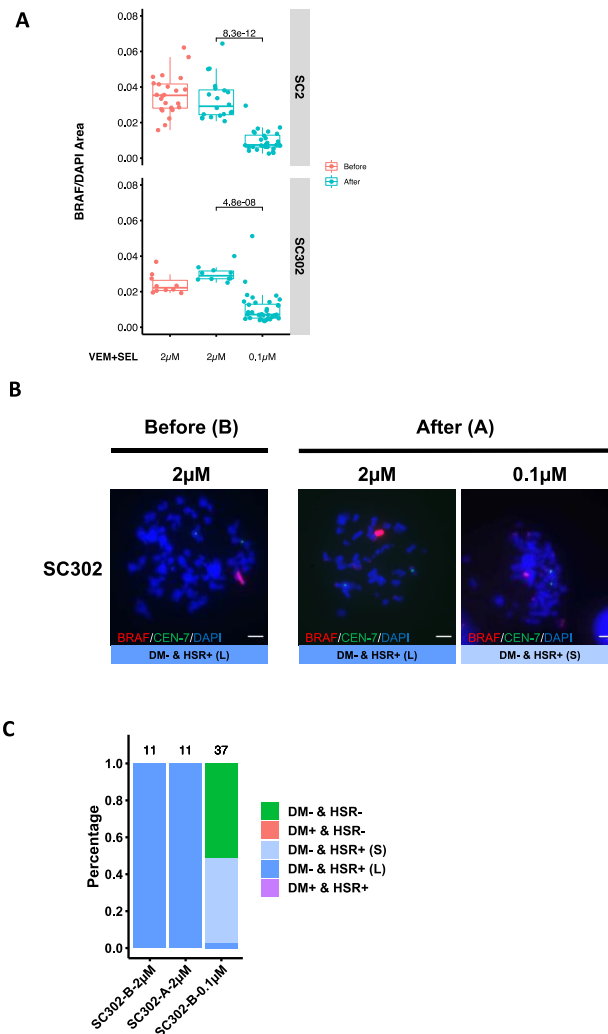
Figure S9. VEM+SEL dose reduction caused BRAF HSR length to shrink in SCs.
Related to Fig. 4. **A**, Normalized BRAF probe area in FISH images before and after dose reduction for quantifying HSR lengths. P-values are based on one-tailed Wilcox test. **B**, Representative FISH images of the DM- & HSR+ clone

26

SC302 before and after dose reduction. C, Karyotype frequencies of clone SC302 before and after dose reduction. S: short HSR. L: long HSR. -B-: Before, -A-: After.

While DM plasticity can be explained by uneven segregation[13–16], HSR plasticity, especially such rapid change in one month, is uncommon during dose challenging – purportedly due to the stability provided by chromosomal integration[51–53]. We thus further analyzed the structural data related to the long to short HSR transition upon dose reduction. To reduce heterogeneity, we used the HSR+ SC2 clone, with its initial long HSR on chromosome 3 (Fig. 2E). In most cells from clone SC2, the post-dose-reduction, short HSR remained located on the same chromosome based on FISH staining. Of note, in some SC2 cells after long term expansion at steady dose (3 months), we detected duplications and/or translocations of smaller versions of the HSR to other chromosomes (with no Chr3 centromere staining), with the concurrent retention of the long HSR on Chr3. Nevertheless, the small HSRs on different chromosomes were either not yet present, or not favored by selection upon dose reduction, in comparison to the shortening of the Chr3 HSR. Taken together, these results demonstrate the de novo evolution of the clonal long HSR both during constant drug dose (duplication), as well as upon dose reduction (shortening) (Fig. 4E-G).

The longer read lengths of optical mapping (OM) aid in the investigation of the structure of such plastic HSRs. The OM data indicated that the BRAF amplicon HSR structure in SC2 is complex and involves tandem duplications and inversions (Fig. 4H and S10A-B). The HSR was integrated at the PAK2 gene locus near the telomere of chr3 (Fig. 4H-I), in line with previous findings that telomeres and telomere-proximal sites are more frequent locations for integration[22,27]. The OM data indicated that the PAK2 locus was duplicated and integration occurred between the two PAK2 copies (Fig. 4H). Increases in the copy number callings based on both OM and WGS data support

27

this PAK2 duplication at the site of integration (Fig. S10C-D). WGS data revealed a consistent

finding and that the joint between chromosome 3 and 7 contained a two-nucleotide non-templated

insertion, supporting a potential role for non-homologs end joining (NHEJ)[54] (Fig. S10E).
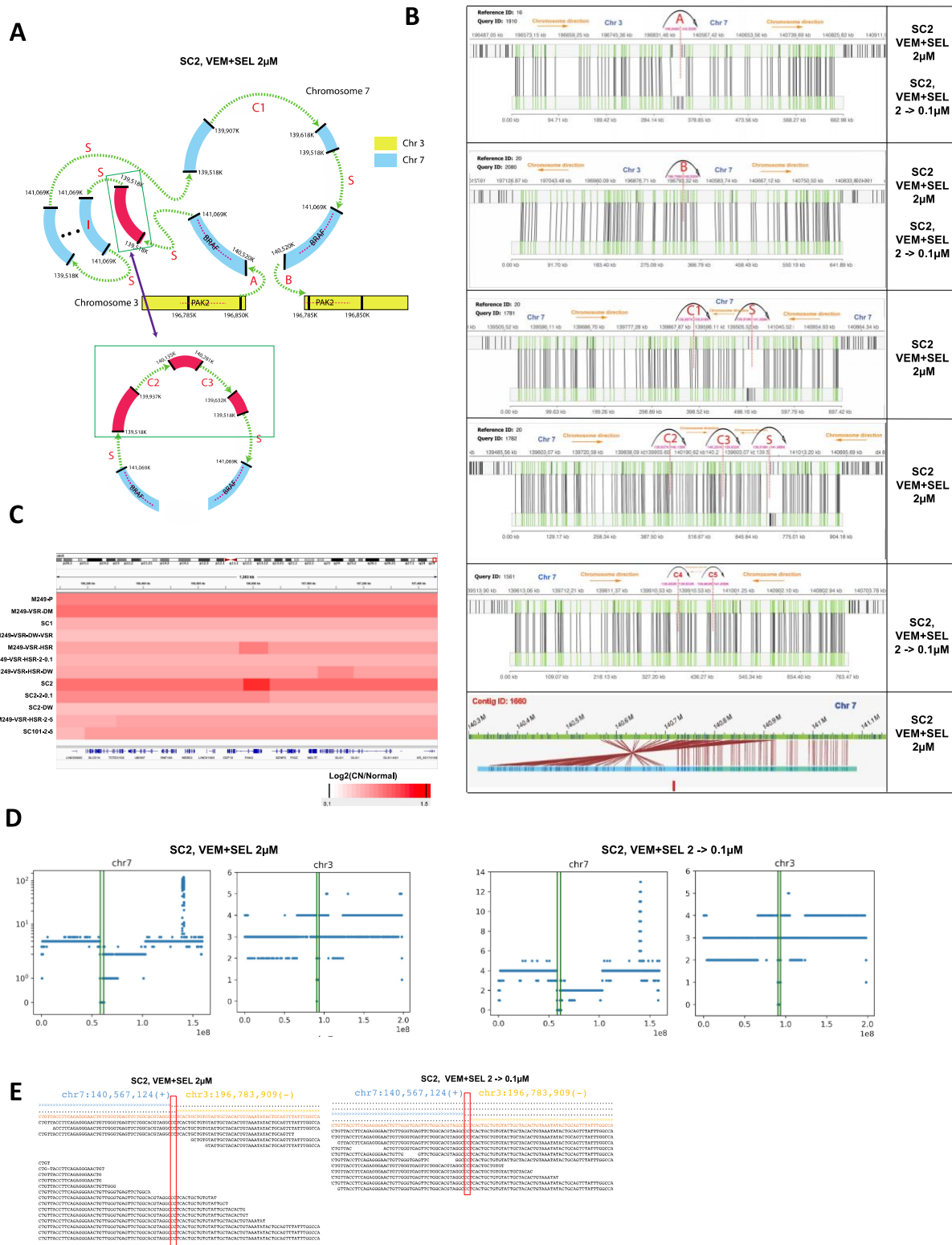
Figure S10. DM- & HSR+ subclone SC2 show alternative BRAF amplicon structure, and its integration on chr3 is supported by PAK2 amplifications. The integration junctions stayed unchanged upon the VEM+SEL dose reduction.

29

Related to Fig. 4. **A-B**, alternative BRAF amplicon structure of SC2 inferred by supporting junctions revealed by optical mapping data. **C**, CNV callings by WGS for multiple M249-VSR variants in this article show DM- & HSR+ subclone SC2 has PAK2 amplification. Its dose reduced version (SC2-2-0.1) and bulk DM- & HSR+ population (M249-VSR-HSR) have weaker and heterogenous PAK2 amplifications. **D**, CNV calling by optical mapping for SC2 before and after dose reduction show decrease of BRAF copy number and PAK2 amplification around chr3 telomere prior to the dose reduction. **E**, BRAF HSR integration junction between chr7 and chr3 before and after dose reduction, revealed SVABA analysis using WGS data.

After VEM+SEL dose reduction, the number of BRAF amplicon repeats decreased, along with the creation of new breakpoints and the generation of a more heterogenous population. However, the integration junction next to PAK2 was preserved in the majority of the cell population (Fig. 4H-I). Overall, the combined OM and WGS data support a potential model of in situ excision of BRAF amplicon repeats, potentially through error and repair mechanisms, in the long to short HSR transitions upon dose reduction (Fig. 4H).

We expanded such finding of DM and HSR plasticity to other MAPKi-resistant subclones from a different cell line, and involving different amplified oncogenes. Clone 3 (C3) of M245 cells harbor RAF1 amplification as DM upon becoming resistance to Trametinib (TRA), while clone 5 (C5) harbor NRAS amplification as an HSR. Drug withdrawal causes copy number decrease in both cases: reducing RAF1 DM number and shortening NRAS HSR (Fig. 4J-K).

While our bulk and single cell clone experiments demonstrate HSR plasticity, we also identified a melanoma cell line with HSR-based focal amplification that had greater genomic stability. The M395-VSR-HSR subline was derived by elevating drug dose over time, and its resistant state was associated with the presence of a BRAF containing HSR. Yet this line did not show shorten or disappeared HSR upon BRAFi+MEKi removal (Fig. S11A-D), which is similar to some previous observations and conclusions about HSR stablility[51,52].
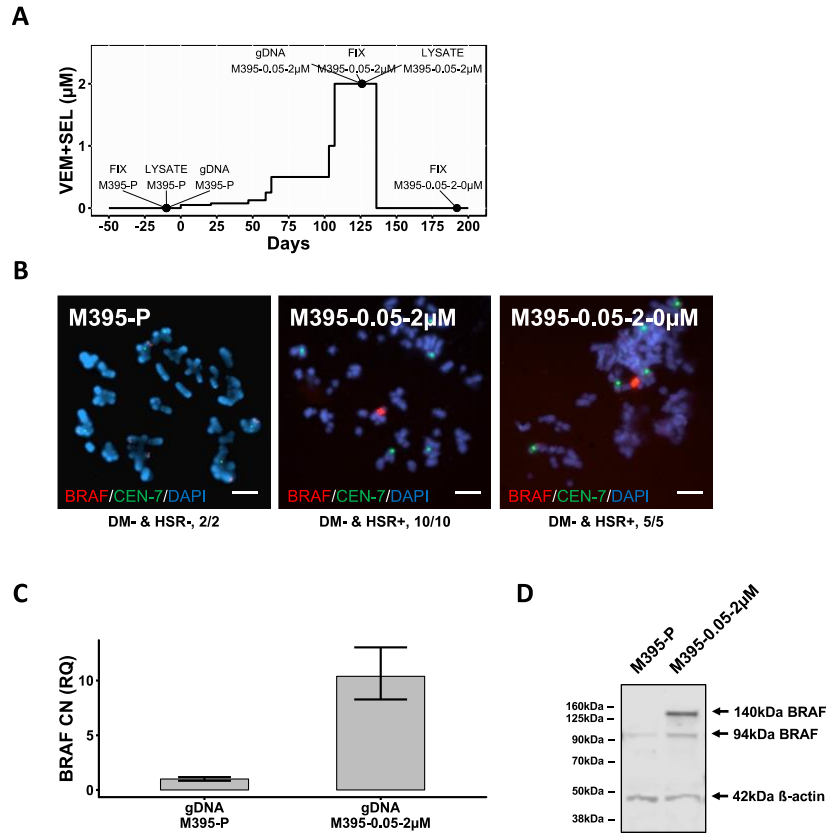
Figure S11. Treatment of M395 melanoma cells with MAPK inhibitors led to BRAF amplification on HSRs co-occurring with BRAF kinase domain duplication. However HSR length did not decrease upon drug withdrawal.
Related to Fig. 4. **A**, VEM+SEL treatment scheme starting from 0.05µM on M395-P (parental) cells. The points when cells were collected for gDNA (genomic DNA), fixation (FIX) and protein lysates (LYSATE) are labeled. **B**, Representative FISH images for fixation time points in (**A**). C, qPCR results of relative BRAF copy number for gDNA collection points in (**A**). CN: copy number. RQ: relative quantity. D, western blot for lysate collection time points in (**A**).

Karyotypic shift from HSRs to DMs carrying BRAF kinase domain duplications upon double-drug dose increase

To further investigate HSR plasticity, we increased the double MAPKi doses applied to the bulk M249-VSR cells at a timepoint when they were predominantly HSR+. Interestingly, this treatment converted the population of predominantly HSR+ cells to predominantly DM+ cells (Fig. 3A-3C, EXP6). Contrary to the expectation that in the higher drug dose the cells would have higher levels of BRAF DNA copy number, we found that the copy number had decreased (Fig. 3D, EXP6).

To investigate this change further, we repeated the experiment using bulk M249-VSR-HSR cells at various time points over the entire HSR-harboring period, roughly 260 days onwards from the beginning of resistance development (Fig. 5A). Four out of five dose-increase experiments resulted in changes of FA types from HSRs to DMs (VS5-1, VS5-2, VS5-3, VS5-4 and VS5-6 (5 sampling points in total)). One out of five resulted in cells that were DM- and HSR- VS5-5) (Fig. 5B-C). Notably, we found that the five DM+ 5μM-resistant samples all expressed a BRAF protein variant with a molecular weight of approximately 140kDa (Fig. 5D). Four of the five DM+ 5μM-resistant samples also expressed the 62kD variant of BRAF, the BRAF inhibitor-resistant splice variant observed in the oscillating dose experiment above. The 140kD size matches a previously reported BRAF variant with a kinase domain duplication (KDD) that leads to BRAF inhibitor resistance [36,55,56]. Based on RT-qPCR using primer pair that spans the BRAF exon 18-10 junction, we discovered that all of the HSR to DM transformed samples carried exon 18-10 junctions, while other cultures, including M249 parental (VS0), M249-HSR cells prior to dose increase (VS2-1, VS2-2, VS2-3 and VS2-4) and M249-HSR cells that showed DM- & HSR- post dose increase (VS5-5), contained none or only a minimal amount of such junctions (Fig. 5E-F). The close to

unity ratio of 18-10 to 9-10 junctions supports that each DM unit contains one KDD region in the

KDD expressing sublines.
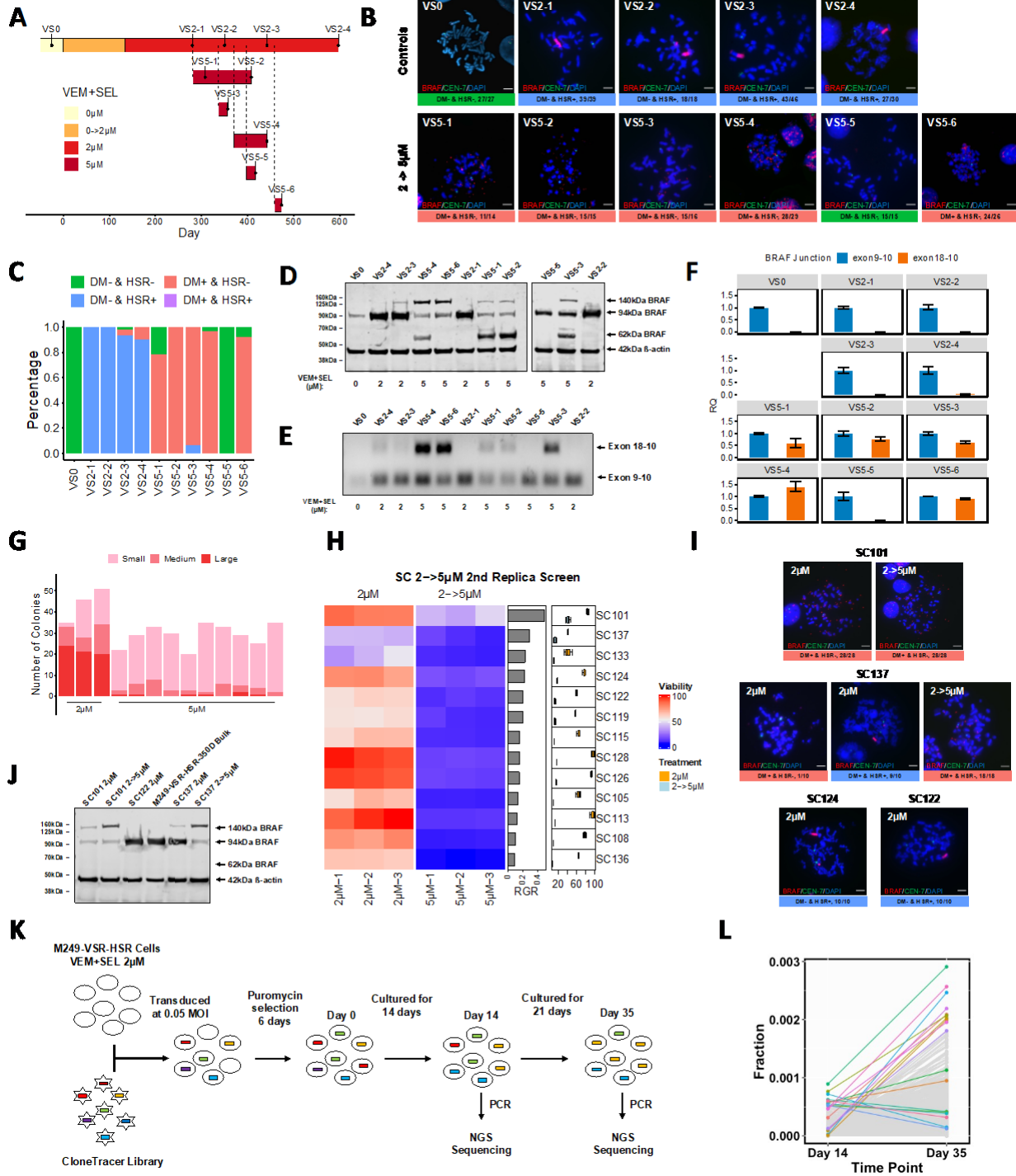
Figure 5. HSR to DM karyotypic switching and BRAF kinase domain duplications mediate resistance to MAPK inhibitor dose increase.

33

A, The relationship between samples examined during the processes of M249 VSR development and VEM+SEL 2µM to 5µM dose increases. **B**, Representative FISH images of all samples in (**A**). **C**, The frequencies of karyotypes for samples in (**A**). **D**, Immunoblot of samples in (**A**), using an antibody that targets the N-terminus of BRAF (12-156aa). The 140kD band is the KDD form, and the 62kD band is the alternatively spliced form of BRAF. **E-F**, qPCR and RT-PCR for samples in (**A**) with primer sets that target BRAF exon 18-10 and exon 9-10 junctions. For RT-qPCR, all values of exon junction 18-10 were normalized to that of exon junction 9-10 of corresponding samples. Error bars represent SEMs around ΔCt values derived by Satterthwaite approximation. **G**, M249-VSR-HSR bulk cells were sorted into single cells on day 322 of the timeline in panel **A** and seeded in 96-well plates. Cells were next treated with either original 2µM (n=3) or 5µM VEM+SEL (n=10) for 12 days. The sizes of the resulting colonies were classified into three categories (Small, Medium and Large) by eye. **H**, second replica screen for M249-VSR-HSR single-cell-derived clones that tolerate VEM+SEL 2 to 5µM dose increase. Rows of the heatmap represent different clones ranked by relative growth rate (RGR), calculated by dividing the mean viability at 5µM by that at 2µM after a six-day culture. Boxplot shows mean and standard deviations of CellTiter-Glo viability (x1000) for each clone on the sixth day (see method). **I**, representative FISH images of selected clones in (**H**) with frequency of each FA mode. **J**, Immunoblot of BRAF in bulk cells and single-cell-derived clones treated with the indicated dose regiments. **K**, Design of the barcode-based clone tracing experiments. Cells were transduced with the lentivirus ClonTracer library on day 318 based on the timeline in (**A**). **L**, Comparison between barcode fractions on Day 14 and Day 35 as depicted in (**K**). Top 10 barcodes by fraction from each sampling time point are highlighted.

We next investigated whether the KDD was developed due to selection of an existing subpopulation or de novo kinase domain duplication after the 2 to 5µM dose increase. Under constant 2µM dose VEM+SEL, the M249-VSR resistant cells were initially primarily DM+ & HSR- (circa day 150), turned primarily DM- & HSR+ with time (circa day 260), and then with additional time reacquired a small percentage of DM+ & HSR- cells (450 days and onwards, Fig. 5A-C). Their late timepoint DM+ & HSR- fractions were 2/46 (4.4%, VS2-3) and 3/30 (10%, VS2-4). This expanding DM+ population could have been the source of KDD that expanded post drug dose increase to 5µM.

To further test if rare DM+ cells were present at earlier times below the level of detection by bulk FISH analysis, we used both single cell sorting and a replica plating approach. First, cells from the earlier-stage M249-VSR-HSR bulk population (322 days) were single cell sorted. This collection of single cell clones was then either treated at the original 2µM dose or at an elevated 5µM dose

of VEM+SEL (Fig. S12A). We found that 3.2% of the single cell clones could grow under 5µM

in a similar manner compared to their counterparts at 2µM (large colonies, Fig. 5G).
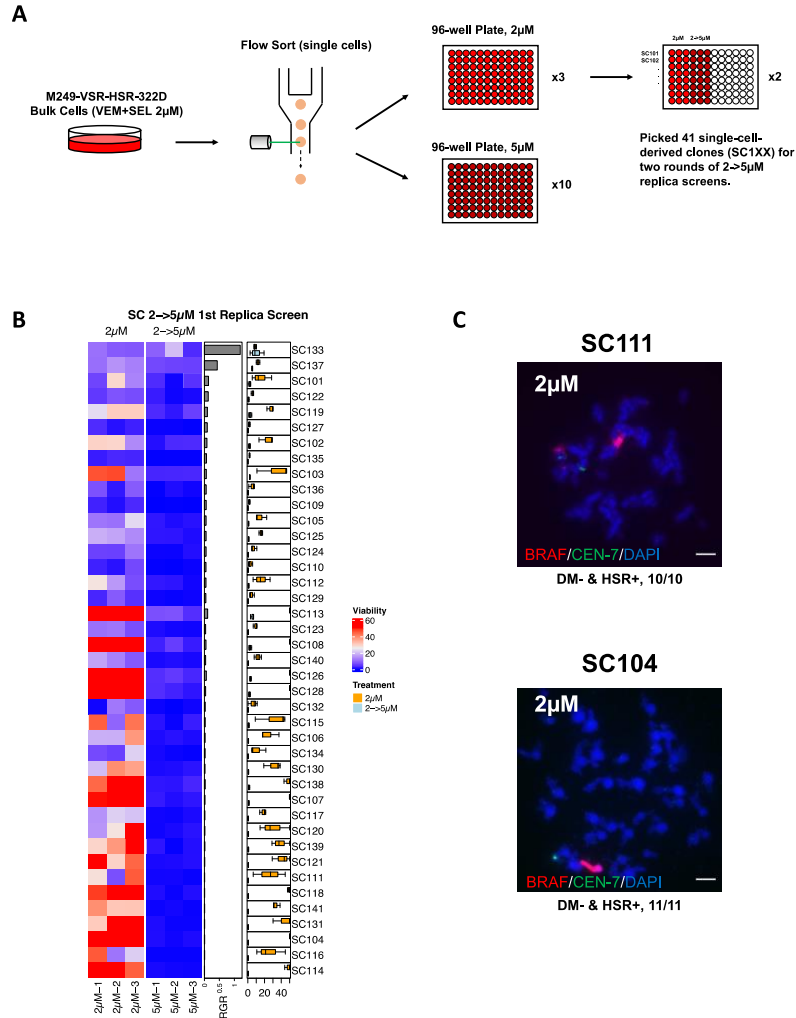
Figure S12. Drug dose challenge characterization of single-cell-derived clones.
Related to Fig 5. **A**, Experimental design to generate single-cell-derived clones (SC1XXs) by sorting M249-VSR-HSR bulk cells on day 322, followed by two rounds of replica screens. **B**, As depicted in (**A**), acute 2 to 5µM VEM+SEL treatment on 41 SC1XXs was used to screen for clones that adapt to 5µM rapidly. The rows of the heatmap represent different SC1XXs ordered by relative growth rate (RGR), calculated by dividing the mean at 5µM by that at 2µM, in descending order. Viability was measured by CellTiter-Glo, and the readings were divided by 1000 followed by capping at 50. **C**, Representative FISH images of two SC1XXs at the lower tail of the heatmap in (**B**).

Next we added a replica plating step. Forty-one single-cell clones derived at 2µM were replica

plated, and then treated in parallel at either the original 2µM dose or the elevated 5µM dose (Fig.

S12A). After two rounds of screening, the clone with the highest relative growth rate (SC101) was revealed to be DM+ & HSR- both before and after the dose increase, with no observed cellular heterogeneity of FA modes (Fig. 5H-I). The second fastest clone (SC137) started with a 10% DM+ & HSR- population, but finished at 100% DM+ & HSR- at the end of the replica plating (Fig. 5H-I). Four other randomly selected SCs from either the near-top of the relative growth rate-sorted list and the bottom of the list displayed no DM+ & HSR- karyotype (SC122, SC124, SC111, SC106, Fig. 5H-I, S12B-C). The two fastest SCs, SC101 and SC137, did harbor BRAF KDD on their DMs according to immunoblot analysis (Fig. 5J). In a second quantitative viability assay, the SC101 and SC137 KDD+ SCs again demonstrated the best ability to tolerate drug dose increases (Fig. S13A). This replica screening result supports that the cells harboring the BRAF KDD containing DMs pre-existed in the bulk population prior to increases in the dual MAPKi dose. These cells were starting to expand in the 2µM drug condition with a relative fitness slightly higher than other cells, but the increase in drug dose sharply increased such fitness advantage. Using a barcode-based clone tracing system (ClonTracer)[57] to keep track of the subpopulations in the bulk M249-VSR-HSR cells (from day 318), we observed that even under the constant 2µM drug dose and at such later timepoints, certain cells did expand faster than others (Fig. 5K-L), indicating the bulk population of cells continues to evolve in regards to its subpopulation distributions.
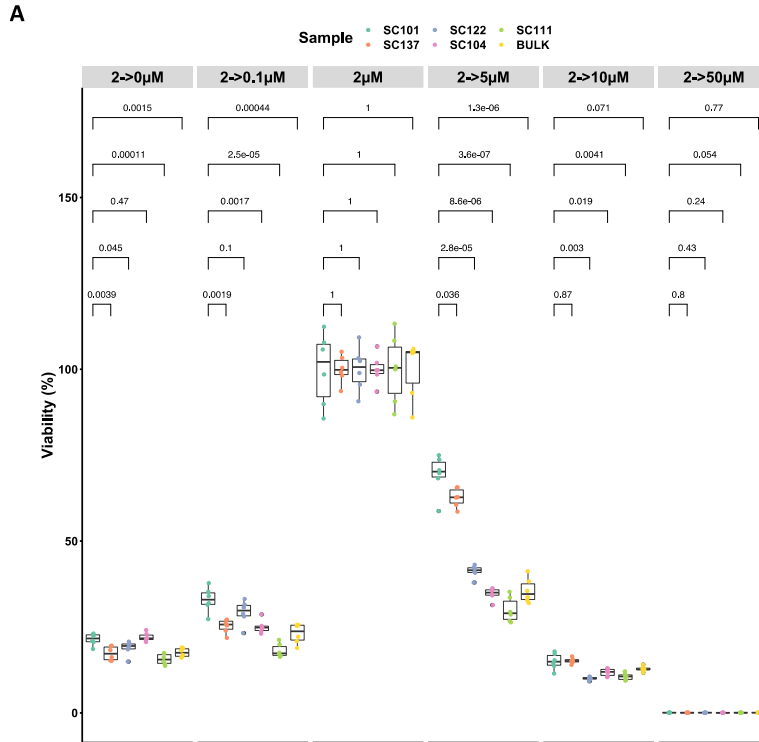
Figure S13. The double-FA-mode (DM+ and KDD+) single-cell-derived clone SC101 tolerates a slightly wider range (definitely 5μM) of MAPK inhibitor dose challenges, compared to other SC1XXs.
Related to Fig 5. **A,** The indicated M249-VSR subclones and M249-VSR-HSR bulk cells initially cultured at 2μM of VEM+SEL were treated with various subsequent inhibitor doses for 4 days, and then their viabilities were measured. All numbers are normalized to the corresponding viabilities at 2μM. P-values are based on one-tailed t test (n = 6).

Interestingly, we did not observe de novo generation of DMs, either KDD-bearing or not, from

BRAF DM- & HSR+ SCs upon performing dual drug (VEM+SEL) escalation (Fig. S14A-B).

Successful HSR to DM transitions have been demonstrated in different cell types, involving

different genes, with corresponding different drug regimens. These reported cases typically

involve the creation of fragile sites or chromothripsis on HSRs[22,26].
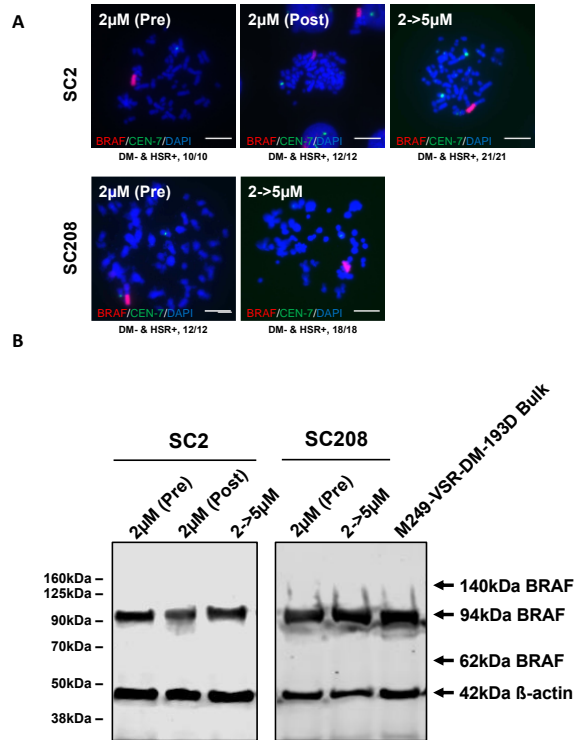
Figure S14. MAPK inhibitor dose escalation applied to HSR-positive SCs did not result in the DM+ & KDD+ genomic configuration.
Related to Fig 5. **A,** Representative FISH pictures of the DM- & HSR+ M249-VSR SCs, SC2 and SC208, with VEM+SEL dose escalated from 2µM to 5µM until they became resistant. **B**, Immunoblot of BRAF samples in (**A**) showing no 140 kDa KDD band after the VEM+SEL dose increase.

Cells preserve BRAF amplicon boundaries under various dose challenges

After learning the plasticities of BRAF-containing DMs and HSRs in response to dose perturbations, we next investigated if amplicon boundaries and junctions changed during these processes. We performed structural variant (SV) analysis on the M249 samples collected after various dose challenges (Fig. 6A) and found that genomic amplification boundaries do not differ substantially regardless of their FA mode, amplicon number, sub-cloning status, nor presence or absence of the KDD selection, supporting a single initial amplicon origin (Fig. 6B). This conclusion is further corroborated by the conserved junctions connecting amplicons in bulk and SC DM+ and HSR+ sublines cultured at full drug dose (Table S1). New junctions were generated during dose decreases and KDD formation, but these alterations did not alter the overall amplification coordinates (Fig. 6B).
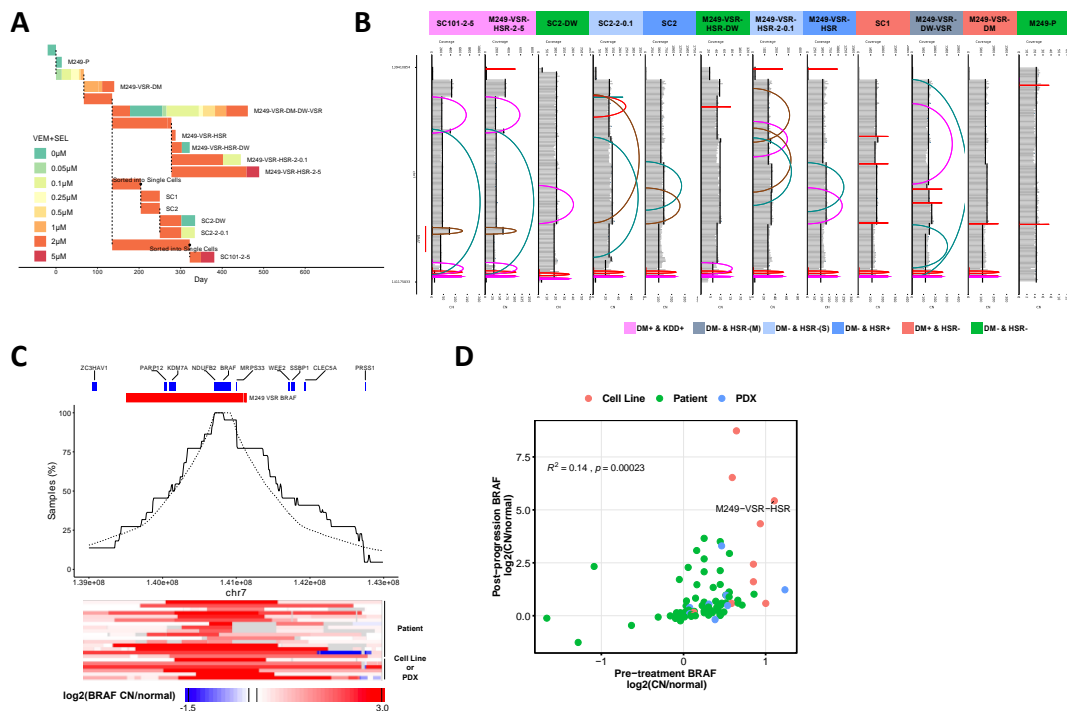
Figure 6. BRAF amplicon boundaries are mostly preserved among switching DM, HSR, short HSR and KDD-DM.

A, Treatment history of M249 samples that have been profiled by WGS. **B**, Amplicon Architect results of BRAF amplicon for M249 samples in (**A**). **C**, A summary of amplification frequencies of regions around BRAF in MAPKi-treated post-progression melanoma samples from previous reports. Solid line represents percentage of samples that pass a log2(BRAF CN post/normal) threshold. Dashed line represents expected frequencies (see Methods). Heatmap shows CNV data at the same region of the line plot, using all samples analyzed. **D**, Correlation between BRAF copy number before MAPKi treatment and that after relapsing from the treatment in melanoma.

We then compared the M249 BRAF amplicon with additional cases in which BRAF focal amplification-mediated MAPKi resistance occurred during inhibitor treatment of patient tumors, patient-derived xenografts (PDXs), and cell lines (Fig 6C-D, Table S2 and S3). In amplicon boundary analysis of this cohort, we did not find evidence for inclusion of co-amplifications adjacent to BRAF (Fig. 6C), different from MYCN and EGFR amplification cases in other tumor types which involve co-amplification of adjacent enhancers[11,12]. We did not observe a relationship between pre-treatment BRAF copy number and its increase post acquirement of resistance (Fig 6D).

Melanoma cells with BRAF amplification-mediated dual BRAFi+MEKi resistance show increased sensitivity to ferroptosis

Given the high plasticity of BRAF amplifications in the M249-VSR series, we next investigated cellular vulnerabilities affiliated with amplification in this dual MAPKi context. Our previous study revealed a correlation between melanoma differentiation stages and sensitivity to pro-ferroptotic drugs[40]. We thus tested if BRAF amplified cells have altered sensitivity to disruption of the repair of oxidized lipids. We tested the sensitivity of the pro-ferroptotic drug RSL3, which targets glutathione peroxidase 4 (GPX4), in the M249-VSR series. We found that both M249-VSR-DM and -HSR are substantially more sensitive to RSL3 compared to M249-P (Fig. 7A). We further found that after drug withdrawal, when the cells have reduced BRAF copy number, M249 cells lose sensitivity reverting to levels closer to the parental cells. Consistently, two additional cases of BRAFi+MEKi-resistance mediated by BRAF amplification (A375-DTR and Mel888-DTR; both lines dabrafenib (BRAFi) + trametinib (MEKi) resistant (DTR)[42]) also showed increased RSL3 sensitivity compared to their parentals. We next confirmed that the RSL3 sensitivity in M249-VSR sublines have the expected characteristics of ferroptosis. Namely that the RSL3 sensitivity is reactive oxidative stress (ROS)-, lipid ROS-, and iron-dependent, as cell death can be rescued by adding reduced glutathione (GSH), the lipophilic antioxidant Trolox, and the iron chelator deferoxamine (DFO) (Fig. 7B-C). We measured lipid ROS levels in M249-P and M249-VSR cells using C11-BODIPY dye and found increased lipid ROS levels upon RSL3 treatment, that was protected by the presence of Trolox (Fig. S15A).

41
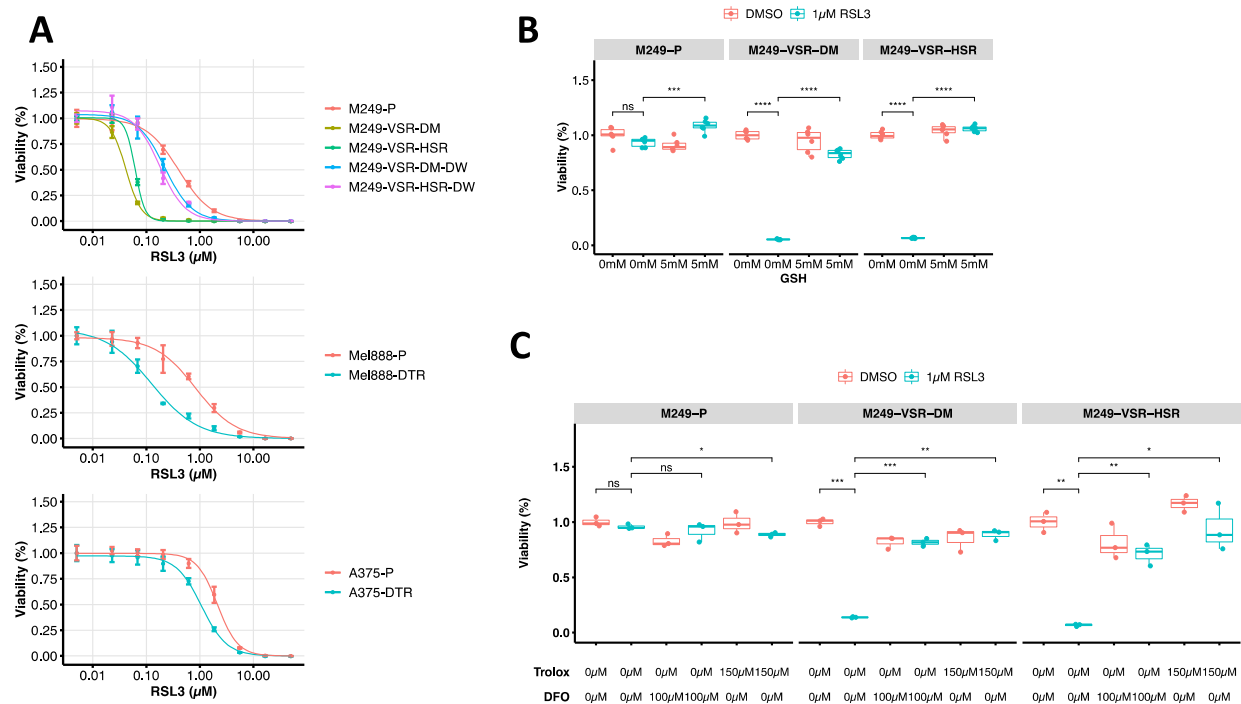
Figure 7. Melanoma cell lines with acquired dual BRAFi+MEKi resistance through BRAF amplification mechanism show sensitivity to ferroptosis inducing agent.
A, Dose-response curves showing increased sensitivity to RSL3 in 3 cases of dual BRAFi+MEKi resistance mediated by BRAF amplification (M249-VSR (both DM and HSR modes of amplification), 888mel-DTR, and A375-DTR) compared to parental sublines. Upon drug withdrawal (DW), the sensitivity of M249-VSR revert to be closer to the original parental case. Three or six replicates. 72 hr treatment. **B-C**, Measurements of percent viable cells with DMSO, RSL3 alone or in combination with the antioxidant reduced glutathione (GSH) (n=6), the lipophilic antioxidant Trolox (n=3) and the iron chelator DFO (n=3). Two-tailed t-test: ns: $p > 0.05$ *: $p \leq 0.05$, **: $p \leq 0.01$, ***: $p \leq 0.001$, ****: $p \leq 0.0001$.

The BRAF-amplified M249 dual MAPKi-resistant cells that are sensitive to the GPX4 inhibitor RSL3 were also sensitive to the pro-ferroptotic drug ferroptocide that targets thioredoxin[58], but were not more sensitive to inhibition of the system x_c^- cystine/glutamate antiporter by Erastin (Fig S15B). Such differential sensitivity to different upstream components of the glutathione synthesis and ferroptosis pathway have been previously observed (e.g. SKMEL28R[40])

We next investigated why these three cell lines with BRAF amplification- and thus MAPK reactivation- mediated resistance demonstrated higher ferroptosis sensitivity compared to their parental sublines. In previous studies, ferroptosis sensitivity in melanoma is associated with innate

or acquired treatment-induced dedifferentiation[40]. However, in our past work, resistance mediated by reactivation of the MAPK pathway through genomic changes (e.g., via NRAS mutation: M249P/R), does not lead to dedifferentiation and changes in ferroptosis sensitivity[40]. We thus analyzed whether the three BRAF-amplified dual MAPKi-resistant cells studied here demonstrated signs of dedifferentiation. Gene expression profiles of RSL3 sensitive M249-VSR (DM and HSR amplification mode), A375-DTR and Mel888-DTR cells (both with HSR mode) do not demonstrate dedifferentiation compared to their parental sublines when their gene expression profiles are projected onto a panel of melanoma lines spanning the full spectrum of differentiation states[40]. By contrast, cell lines M229P/R, M238P/R and SKMEL28P/R, which became resistant through upregulation of RTKs[33], did demonstrate dedifferentiation and increased sensitivity to RSL3 (as tested previously[40]) (Fig. S15C-D). Such findings are also supported by the combination of increases in melanocyte differentiation and pigmentation, decreases in mesenchymal gene set scores, and increases in the melanoma differentiation master regulator MITF in the BRAF amplification samples, and the reverse patterns in the RTK upregulation/dedifferentiation cases (Fig. S15E-H).
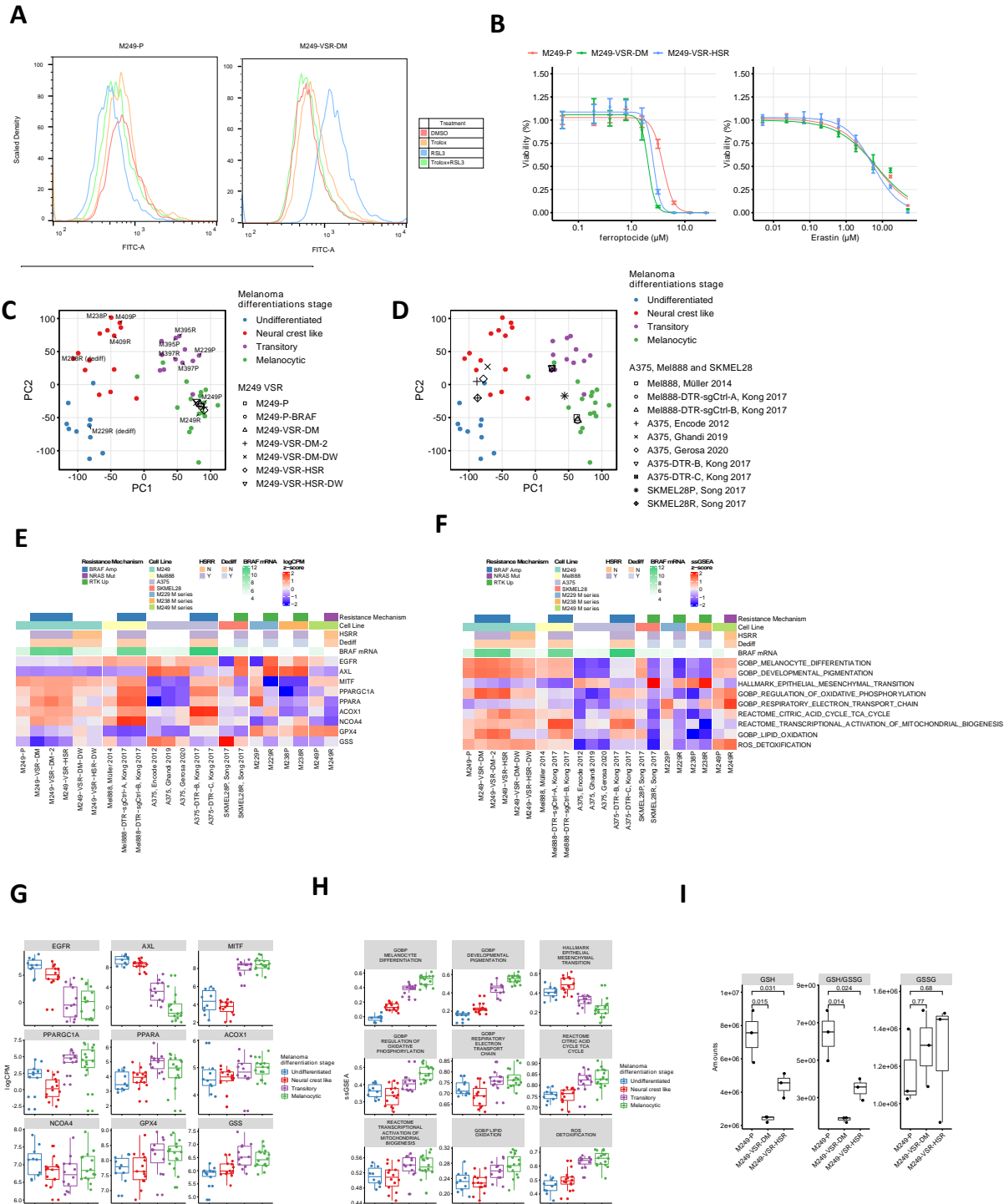
Figure S15. The ferroptosis sensitivity of melanoma cells with BRAF amplification as dual MAPKi resistance mechanism is not due to dedifferentiation.

A, Lipid ROS in M249-P and M249-VSR-DM measured by flow cytometry using lipophilic ROS-sensitive BODIPY™ 581/591 C11 dye upon treatment with or without 1μM RSL3 and 150μM Trolox for 24hr, demonstrating that the lipophilic antioxidant Trolox protects against RSL3-inducded lipid ROS. **B**, Dose-response curve showing increased sensitivity to ferroptocide in in BRAFi+MEKi resistance mediated by BRAF amplification (M249-VSR-DM and -HSR) but no differential sensitivity to Erastin compared to parental cells. Cell viabilities were measured by

44

CellTiter-Glo. Three or six replicates. 72hr treatment. Each experiment was repeated twice. **C**, Projections of the M249-P and M249-VSR variant samples from the current manuscript onto the differentiation trajectory (transcriptomic principal component analysis (PCA)) of the M series of melanoma cell lines from Tsoi et al[40]. The four melanoma differentiation stages are indicated. All M249-P and M249-VSR variants start and remain in the differentiated (melanocytic) cluster upon acquisition of MAPKi resistance. In our past studies, melanoma cells that develop MAPKi resistance through genomic changes that reactivate the MAPK signaling pathway do not dedifferentiate, e.g. M249P/R (NRAS mutation-mediated resistance in this version of single agent BRAFi resistance), do not show different sensitivity to ferroptosis inducing agents, while other cases of resistance due to dedifferentiation (also featured by receptor tyrosine kinase upregulation) are observed, e.g. M229P/R and M238P/R[33,40]. Note that our M249-P and M249-VSR BRAF amplification lines are projected at the same location as the independently derived case of resistance (M249R) and its parental (M249P) pair. In this case resistance is to single agent BRAFi (vemurafenib), with resistance mediated by NRAS mutation[33,40]. Notably, the BRAF-amplified M249-VSR cells are sensitive to RSL3 (Fig. 1A), unlike the NRAS-mutant M249R case[40]. **D**, The same reference PCA-based differentiation state spectrum as in (A), with projections of Mel888-P/-DTR (BRAF amplification), A375-P/-DTR (BRAF amplification) and SKMEL28P/R (dedifferentiation) cell lines. BRAF amplification mediated resistant sublines do not demonstrate gene expression-based signatures of dedifferentiation as compared to their parental pairs. Data was downloaded from the corresponding papers[42,59–63]. **E-F**, mRNA expression and single sample GSEA (ssGSEA)[64] of selected genes and gene sets in the melanoma cell lines before and after establishment of resistance to MAPK inhibitors. Y: YES. N: NO. Amp: amplification. Mut: mutation: RTK Up: receptor tyrosine kinase upregulation. HSRR: <u>H</u>igher <u>s</u>ensitivity to <u>R</u>SL3 in <u>r</u>esistance line. Dediff: dedifferentiation upon resistance. Log10 counts per million (CPM) and ssGSEA z scores were calculated by standardizing within each gene, and for the visualization the values were capped from -2 to +2. **G-H**, selected gene mRNA levels and mRNA-based ssGSEA scores for cell lines in the M series. **I**, Glutathione levels, reduced (GSH), oxidized (GSSG), and ratio (GSH/GSSG), in M249 sublines measured by mass spectrometry. P values were calculated using one-tailed t test.

Upon determination that increased RSL3 sensitivity in these three BRAF amplification cases are not due to dedifferentiation, we then turned our focus to mitochondrial pathways as previous studies have reported that MAPKi resistance can cause melanoma cells to shift their major energy generation program from glycolysis to mitochondrial pathways. This shift then leads to elevated production of ROS and more dependence on ROS detoxifying mechanisms[65–69]. Although ROS were implicated, these prior studies did not assess the change in ferroptosis sensitivity of the resistant sublines. We found that upon acquisition of BRAFi/MEKi resistance M249, Mel888 and A375 all upregulate PPARGC1A (PGC1-α)[65], have distinct but overlapping patterns of upregulation of mitochondrial respiration programs (tricarboxylic acid cycle (TCA), electron transport chain (ETC), oxidative phosphorylation, and mitochondrial biogenesis), and all upregulate lipid oxidation pathways (featured by PPARα and ACOX1[70]). In sum, these changes

may cause higher dependence on glutathione metabolism for lipid detoxification via GPX4, while all cases do not equally upregulate their ROS detoxification pathways (Fig. S15E-F).

In accordance with this last observation, i) expression of the ROS detoxification pathway gene glutathione synthetase (GSS) and inferred activity of the ROS detoxification pathway are downregulated in both dedifferentiation and BRAF amplification cases of MAPKi resistance (Fig. S15G-H), and ii) the levels of reduced glutathione (GSH) are decreased upon both dedifferentiation[40] and upon BRAF amplification (Fig. S15I). We furthermore found that the NCOA4 (nuclear receptor coactivator 4) gene, that mediates the selective autophagic degradation of ferritin[71] is upregulated in both dedifferentiation- and BRAF amplification-mediated MAPKi resistant cells, but is downregulated in NRAS mutation-mediated resistance (where both parental and resistant sublines have similar ferroptosis sensitivity[40]). This observation is in line with a previous study finding that NCOA4 promotes accumulation of cellular labile iron, leading to higher susceptibility to pro-ferroptotic drug[72].

Taken together, although dedifferentiation-mediated MAPKi resistance has distinctions from BRAF amplification-mediated resistance, they both demonstrate increased GPX4 inhibition (RSL3) sensitivity, have a common pattern of downregulated ROS detoxification genes such as GSS, and demonstrate upregulation of the iron homeostasis regulator NCOA4. Furthermore, the absence of such patterns is observed in MAPKi resistance cases that do not demonstrate increased RSL3 sensitivity.

Chapter 3: Discussion

Focal amplifications of oncogenes in either DM- (ecDNA-) or HSR-mode are clinically observed both as a resistance mechanism for inhibitors targeting oncogenes (e.g. erlotinib treatments in glioblastoma[73]) and in the targeted therapy-naïve setting (e.g. MYCN in neuroblastoma[28,74]). The disappearance of oncogene-containing DMs has also been reported upon modeling of oncogene-targeted therapy[75]. While a few-fold amplification of BRAF is sometimes observed in treatment-naïve melanoma tumors[76], higher-fold DM- or HSR-mode focal amplifications are typically seen only following MAPK inhibitor therapy[41,43]. To further elucidate the genomic plasticity enabled by focal amplifications, we developed an expanded version of a BRAF+MEK inhibition and BRAF locus amplification model. This system demonstrated a high degree and broad range of evolutionary plasticity of BRAF amplicon in response to changing drug dose regiments, which can be in part generalized to other amplified MAPK genes mediating resistance (i.e., RAF1 and NRAS). BRAF plasticity was in cases coupled to multiple genomic rearrangement and related mechanisms such as kinase domain duplications and alternative splicing.

In the initial phase of drug resistance to dual BRAF and MEK inhibition, the BRAF amplification appeared via DMs. Under conditions of a stable double drug dose, the population gradually became dominated by an HSR-form of BRAF amplification. Such DM to HSR conversion was also observed in single-cell-derived clones of the M249-VSR cells, supporting that de novo integrations of (potentially agglomerated[46]) DMs did occur in addition to selection of an existing HSR+ population. Such FA mode switch is also supported by the conserved genomic contents between DM and HSR amplicons based on WGS and OM data. This mode switch result adds to reports in the literature for other focally amplified oncogenes in different cancer types. For example, one

study conducted a long-term observation on a non-drug-treated leukemia cell line and saw formation of MYC-carrying HSRs from DMs[25]. Another study proposed a common origin of MYCN DM and HSR in neuroblastoma based on their shared structures[77].

The reproducible observation of the DM to HSR transition led us to hypothesize that DMs carry a higher fitness disadvantage than HSRs during stable conditions. In support of this, we found that an oscillating drug dose could prevent or prolong autosomal integration of the amplicon. This difference in fitness is arguably linked to uneven segregation of DMs[13–16], and the resulting uneven *BRAF* gene copy numbers in daughter cells. During non-stable conditions, cellular heterogeneity provided by uneven segregation can provide a reservoir of cells more adept to grow well in the new conditions. In contrast, during stable drug-dose conditions a reduction in cellular heterogeneity would produce a fitness advantage, which all daughter cells maintaining the optimal *BRAF* gene copy number. We also observed DM numbers tended to decrease during long term stable culture, probably suggesting that a secondary (undetermined) resistance mechanism allowed these cells to depend less on the heterogeneous DMs (Fig. S4A). Taken together, our results along with other findings on the evolution of DMs harboring different oncogenes in different cancer types[25,27,29], support that in non-changing contexts DMs are not a fitness optimized form of amplification, and thus tend to be replaced by other mechanisms such as less heterogeneous chromosomally integrated HSRs.

In contrast, in non-constant conditions, such as the tumor microenvironment or tumors targeted by therapeutics, the uneven segregation of DMs provides an evidence-supported model for tumor heterogeneity that in turn provides tumors the diversity to withstand changes in conditions that

impact fitness[13–16,78]. In the single and double drug withdrawal experiments involving DM+ cells, we saw rapid decreases in the DM copy number (e.g. BRAF or RAF1). It is possible that the rapid changes in DM copy number were due to selection of a pre-existing DM-negative subpopulation or that post-mitosis cells with less DMs due to uneven segregation could have been selected for upon drug withdrawal[13–16]. It is also possible that DMs were exported out of cells through previously observed micronuclei exclusions[79], especially in the single drug withdrawal cases where decreases in DM copy number occurred without appreciable changes in cell viability or growth rates. The single drug withdrawal results also support that dual BRAF and MEK inhibition are required to sustain pressure for high copies of the BRAF gene.

Beyond DM plasticity, our study revealed that 'HSR plasticity' can also be a mode of tumor evolution in response to drug challenge. Dose reduction experiments demonstrate that HSRs can offer somewhat comparable levels of plasticity as DMs. Due to the inherent differences between DM and HSR modes of amplification, this is almost undoubtedly through distinct molecular mechanisms. In more detail, we observed single-cell-derived HSR-containing cell populations that demonstrated dose-tunable BRAF and RAF1 HSR lengths. OM, WGS and FISH data reveal that such length shorting involves reducing the number of amplicon repeats rather than changing integration junctions (Fig. 4A-K). Future work will investigate whether errors and repairs made while replicating and segregating intrachromosomal long HSRs may be generating heterogeneity and thus contributing to this plasticity.

In sum, the single cell clone results support that de novo genetic alterations occur during expansion form a single cell, and/or during the stress of drug withdrawal, thus creating population

heterogeneity and enabling population plasticity. In these cases, selection alone cannot explain the outcome, and clearly genomic instability, in the HSR case potentially mediated by the challenge of replicating adjacent homogeneous regions, is diversifying the population.

The tumor evolutionary and drug resistance plasticity enabled by focal amplifications extended beyond changes in amplicon copy numbers and DM versus HSR modes. In particular we observed two additional parallel mechanisms, i) kinase domain duplication, representing an additional genomic rearrangement mechanism[36,55,56], and ii) activation of an alternative splicing mechanism[35]. Our results indicate cells harboring BRAF KDD-encoded DMs and/or the alternative splicing mechanism can be reproducibly selected from an HSR-predominant population upon drug escalation treatment. The data supports an interpretation in which the cells with KDD-harboring DMs remained within the HSR-harboring cell population, and upon drug escalation the KDD-harboring cells gained a relative fitness advantage. Further research on KDD formation and KDD-mediated resistance could offer therapeutic insights for pan-cancer therapy, as this alteration occurs to many other kinases, such as EGFR and FGFR1 in glioma and lung cancer[80–83]. We also observed the alternative splicing mechanism as a potential method to escape reliance on high DM copy number during an oscillating dose regiment (Fig. 3A-D and S6A-C). The drug resistance provided by the splice variant, arguably lowers the number of DMs required, but maintains the DM-mediated unequal segregation-based heterogeneity.

Therapeutic approaches to target the vulnerabilities of FA-harboring cells are in academic and industry development. Our study demonstrates important challenges, such as mode switching and acquisition of additional genomic rearrangements, that must be co-addressed in these pursuits.

Here we report that BRAF-amplified melanomas relapsed from dual MAPKi treatment show increased ferroptosis sensitivity, which extends the spectrum of ferroptosis sensitivity in melanoma therapy. We found that additional mechanisms, distinct from treatment-induced dedifferentiation and mesenchymal transition, can also generate sensitivity to GPX4 inhibition[40]. This finding links to studies of MAPKi-induced oxidative stress in melanoma. In some melanomas, BRAF V600E activation leads to enhanced glycolysis and reduced oxidative phosphorylation and mitochondrial respiration[65]. However, BRAF inhibition, including acquired resistance to BRAF inhibitors, can switch the energy generation dependency back to oxidative phosphorylation pathway by induction of PPARGC1A and overexpression of other mitochondrial genes [65–68,84,85]. Reactive oxygen species (ROS) productively mediate redox-based energy production in mitochondrial respiration, but they can also damage lipid, protein and DNA.[86] Hence respiring cells need to upregulate detoxification programs to compensate for elevated oxidative stress[69,87]. The imbalance of cellular prooxidative and antioxidative mechanism can lead to cell death[88]. Ferroptosis is one form of cell death that can result from such compromised redox homeostasis, mediated by iron-dependent accumulation of lipid peroxides[89]. More specifically, oxidants such as hydrogen peroxide generated through mitochondria respiration can be converted to hydroxyl radicals through the Fenton reaction in presence of ferrous iron. Then hydroxyl radical can then oxidize membrane phospholipids[90]. Cells need to leverage glutathione synthesis to combat lipid oxidation[91], through the action of genes such as and glutathione synthetase (GSS) and glutathione peroxidase 4 (GPX4).

In our studies, BRAF amplification-mediated MAPKi resistant melanoma cells did not exhibit dedifferentiation. However, they did downregulate GSS and had limited reduced glutathione levels,

which would limit their capacity to detoxify lipid ROS (Fig. S15E-F). They also upregulated the iron homeostasis regulator NCOA4[72,92], similar to other MAPKi parental/resistant melanoma pairs with differential RSL3 sensitivity, consistent with higher vulnerability to ferroptosis induction (Fig. S15E). Relatedly, one previous report found that MAPKi acquired resistance through most MAPK reactivation mechanisms, such as RTK overexpression, NRAS Q61H/*Q61K* mutation, KRAS G12C mutation, BRAF splice variant and BRAF amplification, are all more vulnerable to undergo apoptosis via inhibition of the system x_c^- cystine/glutamate antiporter using HDAC inhibitor, an upstream component of the glutathione synthesis pathway[93]. Our finding complements this by uncovering a different form of cell death, ferroptosis, occurring under a similar MAPKi resistance context, and extends the role of ferroptosis in MAPKi resistance beyond cases of dedifferentiation. Taken together, the melanoma dedifferentiation-independent synthetic lethality between BRAF amplification and ferroptosis identified here provides therapeutic insight for treating BRAF amplified melanomas relapsed from MAPKi treatment.

Collectively, we observed a high degree and broad range of tumor evolution and drug resistance plasticity enabled by or coupled to focal amplifications. Through perturbations by a panel of drug regiment challenges, we observed i) de novo generation of extrachromosomal DMs, ii) de novo integration of DMs into chromosomal HSRs, iii) context-dependent HSR-mediated fitness advantage over DMs, iv) context-dependent DM-mediated fitness advantage over HSRs, v) co-evolution of DMs and a de novo genomic rearrangement creating a kinase domain duplication, vi) co-evolution of DMs and activation of BRAF alternative splicing, vii) propensity to couple secondary resistance mechanisms (KDD and/or alternative splicing) to DMs to reduce the total number of DMs required, and viii) a plasticity of HSRs that compares in some kinetic aspects to

the known plasticity of DMs. Appreciation of the interplay of focal amplification modes with drug regiments and other resistance mechanisms is central to our understanding of tumor evolution and drug resistance, and to developing therapeutic approaches to overcome the resulting plasticity.

Chapter 4: Methods

Cell culture conditions and generation of drug-resistant cell lines

The M249 (RRID: CVCL_D755), M395 (RRID: CVCL_XJ99) and M245 (RRID: CVCL_D754) cell lines are part of the M series melanoma lines established from patient biopsies at UCLA under UCLA IRB approval #02-08-06 and were obtained from Dr. Antoni Ribas[94]. MTG2 and MTG68 cell lines were derived from a patient derived xenograft[95] and were obtained from Dr. Roger Lo. All cells were cultured in RPMI 1640 with L-glutamine (Gibco), 10% (v/v) fetal bovine serum (Omega Scientific), and 1% (v/v) streptomycin (Gibco). All cells were maintained in a humidified 5% CO_2 incubator. BRAF inhibitor vemurafenib and dabrafenib as well as and MEK inhibitor selumetinib and trametinib were obtained from Selleckchem or LC Laboratories. Resistance M249 cell lines were generated by exposing cells to step-wise increasing doses of vemurafenib and selumetinib, similar to the previously described approach[43]. Growth and viability were assayed by staining cells with trypan blue (Sigma-Aldrich) followed by cell counting using Vi-cell XR Cell Viability Analyzer (Beckman Coulter) or by CellTiter-Glo luminescence assay. Doubling times for M249 SCs and bulk cells were calculated by fitting exponential growth curves, and their error bars were derived based on a previously published method[96]. Cells were only sampled for experiments when they show reasonable growth rate at corresponding dose.

Single-cell-derived clones

Resistant subclones were derived by seeding single cells from the bulk population into 96-well plates using FACSAria cell sorter. Doublets are removed by circling the right area in the FSC-height vs area plot. Seeded single cells were then cultured using aforementioned medium or a

modified medium with 20% FBS for two weeks. Culture medium was not changed until clear colonies were observed in some wells. If certain treatments are needed, i.e. double drug dose changes, they are initiated upon seeding the cells. M245 resistance subclones were derived by ring selection[95].

Cytogenetics

Cells were blocked at metaphases by adding colcemid (KaryoMax, Thermo Fisher Scientific) at a final concentration of 0.05µg/ml followed by incubation at 37°C for 6-8 hours. Cells were then fixed using methanol:acetic acid (3:1). FISH slides were prepared by dropping fixed cells in a humid environment following the manufacture's protocol provided by Cytotest and Empire Genomics. FFPE xenograft tumor FISH slides were prepared by pepsin digestion followed by similar procedures of cell line FISH. Colored FISH images were taken and processed using confocal microscope Leica TCS SP8 X. Karyotype categorizations were based on the guidelines in Fig. S1. The fractions under certain images represent the number of cases for corresponding karyotype divided by total number of cases analyzed. If not otherwise mentioned, scale bars in FISH images represent 10µm. Centromere probe names are abbreviated as CEN-x. DM numbers were quantified by directly counting the number of features in the FISH images or by using ecDNA quantification tool EcSeg[97]. HSR lengths were quantified by dividing the probe area by chromosomal DAPI area in metaphases. The staining areas were calculated using ImageJ. Cells fixed by the same procedure were also used for G-banding. G-banded metaphase spreads were photographed using 80i Nikon Microscope and Applied Spectral Imaging (ASI) Karyotyping system. A minimum of ten metaphases were karyotyped.

qPCR-based BRAF copy number assay

qPCRs for BRAF genomic DNA (gDNA) copy number measurement were performed by combining samples with PowerUp SYBR Green Master Mix (Applied Biosystems) in Optical 96-Well Reaction Plates (Applied Biosystems) with three technical replicates for each sample. Plates were then read by 7500 Real-Time PCR System (Applied Biosystems) using the standard cycling mode. Input templates for all samples were genomic DNAs extracted using DNeasy Blood & Tissue Kits (Qiagen). Unless specified, all qPCR runs used M249 parental as the reference sample and GAPDH as the endogenous control. Error bars represent t-distribution-based 95% confidence intervals from triplicates: $RQ_{max/min} = 2^{-\Delta\Delta Ct \pm t_{0.05,df}*SE}$. RQ: relative quantity. Ct: threshold cycle. df: degree of freedom. SE: sample standard error. All primers were ordered from Eurofins Scientific and their sequences are shown below.

BRAF Forward: 5'-TTTAGAACCTCACGCACCCC-3' (intron 2)

BRAF Reverse: 5'-TGTTGTAGTTGTGAGCCGCA-3' (intron 2)

GAPDH Forward: 5'-CTGGCATTGCCCTCAACG-3'

GAPDH Reverse: 5'-AGAAGATGAAAAGAGTTGTCAGGGC-3'

Comparative genomic hybridization and low-pass whole genome sequencing

Genomic DNA of M249-P and M249-VSR cells were isolated by using DNeasy Blood & Tissue Kits (Qiagen). Samples were run on Agilent 6x80K array. The raw data was then processed by Cytogenomics software (Agilent Technologies). Nested genomic regions were flattened and .seg files were generated through R programming, followed by data visualization in IGV[98]. Regions

with large copy number changes were identified by comparing every segment in M249-VSR with the corresponding segment in M249-P. The same genomic DNAs were sent to PacGenomics for low-pass WGS with coverage of 0.04. Library was prepared using KPA DNA Library Preparation Kit. Sequencing was performed on Illumina NextSeq 500 using 75 bp paired end reads (2 x 75 bp). CNV was inferred using Ginkgo[99], which contains a step that used bowtie[100] to align raw reads to hg19 genome.

Whole genome sequencing, copy number and structural variant calling of M249 series

Genomic DNA of M249-P and M249-VSR sublines were extracted by DNeasy Blood & Tissue Kits. The samples underwent whole-genome sequencing library preparation and then sequenced on Illumnia Novaseq S1 at 2x150 and 10-15x coverage. Raw reads in fastq files were aligned to hg38 using BWA-MEM[101]. The duplicated reads were marked by MarkDuplicates (Picard) tool from GATK[102]. Next, CNV callings were performed using CNVkit[103] with flat normal as the control. Segmentation was performed using hmm-tumor method. CNVkit results were used the input for AmpliconArchitect[104]. The same genomic region chr7:139410000-141180000, which corresponds to BRAF amplicon, was used as the seed interval for all M249 samples when running AmpliconArchitect. Structural variants were also called using SVABA[105] for analyzing break points and integration junctions.

AmpliconReconstructor analysis

AmpliconArchitect-generated breakpoint graphs were first converted to in silico digested optical map segments. AmpliconReconstructor[46] (https://github.com/jluebeck/AmpliconReconstructor)

was then run with default settings on the breakpoint graph segments and the assembled Bionano contigs from the Bionano Genomics optical genome map de novo assembly pipeline. From the collection of reconstructed breakpoint graph paths present, we identified circular or non-circular paths representing the ecDNA or HSR structures. Resulting structures were visualized with CycleViz (https://github.com/jluebeck/CycleViz).

FaNDOM analysis

Optical map alignment of Bionano contigs to the reference genome and Bionano raw molecules to the reference genome was performed with FaNDOM[106] (https://github.com/jluebeck/FaNDOM). Default settings were used in both alignment tasks. Resulting alignments were passed to the Bionano SV detection module 'wrapper_contigs.py' to estimate genomic breakpoints. Alignments were visualized with the MapOptics[107] software.

RNA-seq analysis

Total RNA was isolated from M249-P and M249-VSR cells by using RNeasy Plus Mini Kit (Qiagen). Samples were sequenced on HiSeq3000 (Illumina) at 150bp paired-end. Raw data was then processed using Toil pipeline to output transcripts per million (TPM), including the STAR algorithm that aligned raw reads to GRCh38 genome[108,109]. Following data trimming and log transformation, visualizations were done in R. For calculating allele frequencies of BRAF V600E, all RNA-seq fastq files were aligned using STAR, and the resultant bam files were processed according to GATK RNA-seq short variant discovery best practices until the step of haplotype calling[110]. For visualization, we loaded base quality score recalibrated bam files to IGV.

Immunoblotting and antibodies

Cell lysates were prepared by using mRIPA buffer supplemented with PMSF, leupeptin and aprotinin. Western blots were performed using following antibodies: beta-actin (AC-15, Sigma-Aldrich), beta-actin (13E5, Cell Signaling Technology), BRAF (F-7, Santa Cruz Biotechnology), BRAF (C-19, Santa Cruz Biotechnology), Goat anti-Rabbit secondary antibodies (IRDye 680RD, LI-COR), Goat anti-Mouse secondary antibodies (IRDye 800CW, LI-COR). Images were directly output by Odyssey CLx Imaging System (LI-COR).

Reverse transcriptase (RT) -PCR and -qPCR

Total RNA was extracted from fresh cells using RNeasy Plus Mini Kit (Qiagen). Reverse transcriptions were then performed by using SuperScript VILO cDNA Synthesis Kit (Invitrogen). cDNA was then used for PCR and qPCR. Primers for detecting exon18-10 and exon9-10 junctions were the same as what previously published[36]. The regular PCR was performed using Phusion High-Fidelity PCR Master Mix with HF Buffer (New England Biolabs). The PCR products that targeted exon18-10 and exon9-10 were then combined for each sample and run on 2% agarose gel. For qPCR, each sample was combined separately with PowerUp SYBR Green Master Mix (Applied Biosystems) and loaded on Optical 96-Well Reaction Plates (Applied Biosystems) in triplicate. Plates were then read by 7500 Real-Time PCR System (Applied Biosystems) using the standard cycling mode.

Replica Plating Screen for DM-KDD Subpopulation

Each of 41 Single cells derived clones (SCs) of M249-VSR-HSR cells (cultured at 2μM VEM+SEL) was seeded in 6 wells of 96-well plates with the same cell number per well. Three wells of each clone were treated by 5μM VEM+SEL white the other three stayed at 2μM. After 6 days, cell viabilities were measured by CellTiter-Glo Luminescent Cell Viability Assay. 13 of 41 SCs were picked for a second round of the dose increase screen to confirm the findings. The viability of SCs was visualized by heatmaps using the R package ComplexHeatmap[111].

Barcode-Based Clone Tracing

ClonTracer Barcoding Library[57] was purchased from Addgene. The plasmid pool was expanded by electroporation transformation. Lentivirus was made by transfecting 293T cells. M249-VSR-HSR cells were tested for their puromycin dose-response and multiplicity of infection curves. For the actual infection, 54 million M249 HSR cells were spin-infected in 12 well plate with 8μg/ml polybrene, followed by a six-day puromycin (0.3μg/ml) selection. Day 0 refers to the end of the selection. Next, cells underwent a standard culture growth period with kinase inhibitors present until the genomic DNA collection points on day 14 and day 35. The sequencing library was prepared by PCR amplification of barcode regions using the primer sequence provided by the manufacturer. The libraries were paired-end sequenced on Illumina NextSeq 500 at 75bp read length.

Analysis of copy number data for MAPKi treated melanoma

MAPKi treated melanoma copy number profiles from multiple previous studies were downloaded and compiled. The list of studies[5,22,33,36,43,112–117], data types and softwares for CNV calling can be

found in Table S2. Table S3 contains a subset of sample in S1 that have paired pre-treatment and post-progression time points. When the actual normal samples are not available for certain patients, flat normals were used to call CNV. Gene level copy numbers of BRAF were determined by averaging all length normalized segments in BRAF genomic region after removing the gaps.

Simulation of BRAF amplification boundaries

For Fig.6C, the expectation of amplicon boundaries around BRAF was simulated using a method from previous study[11]. Briefly, to construct the solid line, real copy number profiles of treated melanoma samples used include those that have both pre-treatment and post-progression time points with log2(BRAF CN post/pre)>0.75 and log2(BRAF CN post/normal) > 1.3 as well as those don't have pre-treatment data available and log2(BRAF CN post/normal)>1.7 were used. We have confirmed all selected samples have focal BRAF amplification instead of arm level. For the dashed line, random amplicons were generated by shifting each of real BRAF amplicon boundaries multiple times but still encompass BRAF gene. The boundaries are sometimes defined after merging nearby CNV segments with log2 differences within 1 and gaps smaller than 1Mb. The genome was binned at 10kb size. For each bin, amplification frequency is defined by the percentage of samples that have log2(BRAF CN post/normal)>1.3.

Dose response curve

The dose response curve of ferroptosis inducing agents (RSL3: Cayman Chemical, Erastin: Selleckchem and Ferroptocide: gift from Paul J. Hergenrother[58]) was performed by seeding appropriate number of cells on day 0 in 96-well plates, treating cells on day 1 with corresponding

drugs and reading the plates on day 4 for viability using CellTiter-Glo luminescent assay. If not otherwise mentioned, resistance cells were maintained in full dose of MAPK inhibitors throughout the dose response experiments to keep the BRAF amplifications. Seeding density for each cell line was determined by using the same assay and the same experimental length with multiple cell number titrations. The dose series were generated by serial dilutions. All drugs used for dose response curves were dissolved in DMSO. DMSO toxicity was performed on the cell lines to determine the appropriate DMSO concentration (0.05%), which was used in all doses. The resulting values from viability assays were normalized to the zero dose condition after subtracting background (wells with no cells). The curve fittings were performed by using three-parameter model in drc package[118].

Viability assay for inducing and protecting from ferroptosis

6000 cells were seeded per well in 96-well plates and treated with ferroptosis inducing agents in combination with vehicle, GSH, Trolox or DFO next day. CellTiter-Glo luminescence was assessed 24hr after treatment. For quantification, all values are normalized to vehicle conditions. Resistance cells were maintained in full dose of MAPK inhibitors throughout the treatments to keep the BRAF amplifications.

ROS measurements

In 12-well plates, 80000 M249-P and M249-VSR-DM cells were seeded per well and treated with next day with RSL3 in combination with Trolox or vehicle. Resistance cells were maintained in full dose of MAPK inhibitors keep the BRAF amplifications. After 24hr, CM-H2DCFDA dye

(Invitrogen C6827) was added to each well and incubated for another 20min at 37°C. Cells were then washed with PBS, harvested by trypsinization, suspended in 250ml PBS and filtered through cell strainers. The samples were analyzed with BD LSRII Analytic Flow Cytometer at the excitation wavelength of 488-nm.

Metabolomics-based Glutathione measurement

Appropriate number of cells were seeded 10cm dishes for 72hr growth to reach 80% confluency. MAPKi-resistant cells were maintained in full dose of VEM+SEL keep the BRAF amplifications. On the day of collection, cells were rinsed with ice-cold 150mM NH4AcO at pH 7.3, incubated with 80% MeOH at -80°C for 20 minutes, scrapped off from the plates and transferred to Eppendorf tubes. Cells are then vortexed for 10 seconds and centrifuged at 16000g for 15 minutes at 4°C. The supernatants were transferred to glass vial and dried in Genevac EZ-2 Elite evaporator at 30°C to obtain metabolite extracts.

Dried metabolites were resuspended in 50% acetonitrile (ACN):water and 1/10th was loaded onto a Luna 3um NH2 100A (150 × 2.0 mm) column (Phenomenex). The chromatographic separation was performed on a Vanquish Flex (Thermo Scientific) with mobile phases A (5 mM NH4AcO pH 9.9) and B (ACN) and a flow rate of 200 µl/min. A linear gradient from 15% A to 95% A over 18 min was followed by 9 min isocratic flow at 95% A and re-equilibration to 15% A. Metabolites were detection with a Thermo Scientific Q Exactive mass spectrometer run with polarity switching (+3.5 kV/− 3.5 kV) in full scan mode with an m/z range of 70-975 and 70.000 resolution. TraceFinder 4.1 (Thermo Scientific) was used to quantify the targeted metabolites by area under the curve using expected retention time and accurate mass measurements (< 5 ppm).

Values were normalized to protein content of extracted material. Data analysis was performed using in-house R scripts.

Data analysis of melanoma dedifferentiation, ferroptosis and ROS related program

Raw RNAseq data of Mel888, Mel888-DTR, A375, A375-DTR, SKMEL28P, SKMEL28R and M series cell lines were downloaded from corresponding GEO accessions[40,42,59–63]. The data was processed through Toil[109] to obtain RSEM[119] expected counts and normalized by log-transformed counts per million (logCPM) approach. Principle component analysis (PCA) was performed using mean-centered logCPM values of M series cell lines and serve as the framework, on which RNAseq data of other samples were projected onto for determining their dedifferentiation stages. The scores of selected gene sets for the parental/resistance-paired cell lines was calculated using the single sample gene set enrichment analysis (ssGSEA) method in GSVA R package[120]. Nearly are gene sets were taken from MSigDB[121,122] except for ROS detoxifying gene sets which was made by combining i) a subset of detoxifying genes (a combination of multiple detoxifying gene sets in MSigDB) that correlate well (Pearson correlation > 0.4) with the dedifferentiation trajectory scores of M series samples and ii) top 8 genes that downregulate upon knocking down PGC1α in A375 cells[69].

Reference

1. Hanahan, D. & Weinberg, R. A. Hallmarks of cancer: The next generation. *Cell* vol. 144 646–674 (2011).

2. Collins, S. & Groudine, M. Amplification of endogenous myc-related DNA sequences in a human myeloid leukaemia cell line. *Nature* (1982) doi:10.1038/298679a0.

3. Beroukhim, R. *et al.* The landscape of somatic copy-number alteration across human cancers. *Nature* **463**, 899–905 (2010).

4. Ercan, D. *et al.* Amplification of EGFR T790M causes resistance to an irreversible EGFR inhibitor. *Oncogene* **29**, 2346–2356 (2010).

5. Shi, H. *et al.* Melanoma whole-exome sequencing identifies V600E B-RAF amplification-mediated acquired B-RAF inhibitor resistance. *Nat. Commun.* **3**, 724–728 (2012).

6. Wu, S. *et al.* Circular ecDNA promotes accessible chromatin and high oncogene expression. *Nature* (2019) doi:10.1038/s41586-019-1763-5.

7. Cox, D., Yuncken, C. & Spriggs, A. I. Minute Chromatin Bodies in Malignant Tumours of Childhood. *Lancet* **286**, 55–58 (1965).

8. Hamkalo, B. A., Farnham, P. J., Johnston, R. & Schimke, R. T. Ultrastructural features of minute chromosomes in a methotrexate-resistant mouse 3T3 cell line. *Proc. Natl. Acad. Sci. U. S. A.* **82**, 1126–1130 (1985).

9. Harley, C. B. *et al.* Nucleic Acids Research. **16**, 7269–7285 (1988).

10. Zhu, Y. *et al.* Oncogenic extrachromosomal DNA functions as mobile enhancers to globally amplify chromosomal transcription. *Cancer Cell* (2021) doi:10.1016/j.ccell.2021.03.006.

11. Helmsauer, K. *et al.* Enhancer hijacking determines extrachromosomal circular MYCN

amplicon architecture in neuroblastoma. *Nat. Commun.* (2020) doi:10.1038/s41467-020-19452-y.

12. Morton, A. R. *et al.* Functional Enhancers Shape Extrachromosomal Oncogene Amplifications. *Cell* (2019) doi:10.1016/j.cell.2019.10.039.

13. Levan, A. & Levan, G. Have double minutes functioning centromeres? *Hereditas* (1978) doi:10.1111/j.1601-5223.1978.tb01606.x.

14. Lundberg, G. *et al.* Binomial mitotic segregation of MYCN-carrying double minutes in neuroblastoma illustrates the role of randomness in oncogene Amplification. *PLoS One* **3**, (2008).

15. Turner, K. M. *et al.* Extrachromosomal oncogene amplification drives tumour evolution and genetic heterogeneity. *Nature* **543**, 122–125 (2017).

16. Verhaak, R. G. W., Bafna, V. & Mischel, P. S. Extrachromosomal oncogene amplification in tumour pathogenesis and evolution. *Nat. Rev. Cancer* **19**, 283–288 (2019).

17. Biedler, J. L. & Spengler, B. A. A novel chromosome abnormality in human neuroblastoma and antifolate-resistant chinese hamster cell lines in culture. *J. Natl. Cancer Inst.* **57**, 683–695 (1976).

18. Toledo, F., Le Roscouet, D., Buttin, G. & Debatisse, M. Co-amplified markers alternate in megabase long chromosomal inverted repeats and cluster independently in interphase nuclei at early steps of mammalian gene amplification. *EMBO J.* (1992) doi:10.1002/j.1460-2075.1992.tb05332.x.

19. Ma, C., Martin, S., Trask, B. & Hamlin, J. L. Sister chromatid fusion initiates amplification of the dihydrofolate reductase gene in Chinese hamster cells. *Genes Dev.* (1993) doi:10.1101/gad.7.4.605.

20. Shimizu, N., Shingaki, K., Kaneko-Sasaguri, Y., Hashizume, T. & Kanda, T. When, where and how the bridge breaks: Anaphase bridge breakage plays a crucial role in gene amplification and HSR generation. *Exp. Cell Res.* (2005) doi:10.1016/j.yexcr.2004.09.001.

21. Kaufman, R. J., Brown, P. C. & Schimke, R. T. Amplified dihydrofolate reductase genes in unstably methotrexate-resistant cells are associated with double minute chromosomes. *Proc. Natl. Acad. Sci. U. S. A.* (1979) doi:10.1073/pnas.76.11.5669.

22. Shoshani, O. *et al.* Chromothripsis drives the evolution of gene amplification in cancer. *Nature* (2021) doi:10.1038/s41586-020-03064-z.

23. Rausch, T. *et al.* Genome sequencing of pediatric medulloblastoma links catastrophic DNA rearrangements with TP53 mutations. *Cell* (2012) doi:10.1016/j.cell.2011.12.013.

24. Carroll, S. M. *et al.* Double minute chromosomes can be produced from precursors derived from a chromosomal deletion. *Mol. Cell. Biol.* **8**, 1525–33 (1988).

25. Von Hoff, D. D., Forseth, B., Clare, C. N., Hansen, K. L. & VanDevanter, D. Double minutes arise from circular extrachromosomal DNA intermediates which integrate into chromosomal sites in human HL-60 leukemia cells. *J. Clin. Invest.* **85**, 1887–1895 (1990).

26. Coquelle, A., Rozier, L., Dutrillaux, B. & Debatisse, M. Induction of multiple double-strand breaks within an hsr by meganuclease I-SceI expression or fragile site activation leads to formation of double minutes and other chromosomal rearrangements. *Oncogene* (2002) doi:10.1038/sj.onc.1205880.

27. Ruiz, J. C. & Wahl, G. M. Chromosomal destabilization during gene amplification. *Mol. Cell. Biol.* (1990) doi:10.1128/mcb.10.6.3056.

28. Koche, R. P. *et al.* Extrachromosomal circular DNA drives oncogenic genome remodeling

in neuroblastoma. *Nature Genetics* (2020) doi:10.1038/s41588-019-0547-z.

29.   Kaufman, R. J., Brown, P. C. & Schimke, R. T. Loss and stabilization of amplified

        dihydrofolate reductase genes in mouse sarcoma S-180 cell lines. *Mol. Cell. Biol.* (1981)

        doi:10.1128/mcb.1.12.1084.

30.   Mitelman, F., Johansson, B. & Mertens, F. Mitelman Database of Chromosome

        Aberrations and Gene Fusions in Cancer. (2019).

31.   The Cancer Genome Atlas (TCGA). *Online*.

32.   Flaherty, K. T. *et al.* Combined BRAF and MEK inhibition in melanoma with BRAF

        V600 mutations. *N. Engl. J. Med.* (2012) doi:10.1056/NEJMoa1210093.

33.   Nazarian, R. *et al.* Melanomas acquire resistance to B-RAF(V600E) inhibition by RTK or

        N-RAS upregulation. *Nature* **468**, 973–977 (2010).

34.   Johannessen, C. M. *et al.* COT drives resistance to RAF inhibition through MAP kinase

        pathway reactivation. *Nature* **468**, 968–972 (2010).

35.   Poulikakos, P. I. *et al.* RAF inhibitor resistance is mediated by dimerization of aberrantly

        spliced BRAF(V600E). *Nature* (2011) doi:10.1038/nature10662.

36.   Kemper, K. *et al.* BRAF V600E Kinase Domain Duplication Identified in Therapy-

        Refractory Melanoma Patient-Derived Xenografts. *Cell Rep.* (2016)

        doi:10.1016/j.celrep.2016.05.064.

37.   Paraiso, K. H. T. *et al.* PTEN loss confers BRAF inhibitor resistance to melanoma cells

        through the suppression of BIM expression. *Cancer Res.* (2011) doi:10.1158/0008-

        5472.CAN-10-2954.

38.   Wagle, N. *et al.* Dissecting therapeutic resistance to RAF inhibition in melanoma by

        tumor genomic profiling. *J. Clin. Oncol.* (2011) doi:10.1200/JCO.2010.33.2312.

39. Sun, C. *et al.* Reversible and adaptive resistance to BRAF(V600E) inhibition in melanoma. *Nature* **508**, 118–122 (2014).

40. Tsoi, J. *et al.* Multi-stage Differentiation Defines Melanoma Subtypes with Differential Vulnerability to Drug-Induced Iron-Dependent Oxidative Stress. *Cancer Cell* (2018) doi:10.1016/j.ccell.2018.03.017.

41. Xue, Y. *et al.* An approach to suppress the evolution of resistance in BRAF V600E-mutant cancer. *Nat. Med.* **23**, 929–937 (2017).

42. Kong, X. *et al.* Cancer drug addiction is relayed by an ERK2-dependent phenotype switch. *Nature* **550**, 270–274 (2017).

43. Moriceau, G. *et al.* Tunable-Combinatorial Mechanisms of Acquired Resistance Limit the Efficacy of BRAF/MEK Cotargeting but Result in Melanoma Drug Addiction. *Cancer Cell* **27**, 240–256 (2015).

44. L'Abbate, A. *et al.* MYC-containing amplicons in acute myeloid leukemia: genomic structures, evolution, and transcriptional consequences. *Leukemia* (2018) doi:10.1038/s41375-018-0033-0.

45. Kim, H. *et al.* Extrachromosomal DNA is associated with oncogene amplification and poor outcome across multiple cancers. *Nat. Genet.* (2020) doi:10.1038/s41588-020-0678-2.

46. Luebeck, J. *et al.* AmpliconReconstructor integrates NGS and optical mapping to resolve the complex structures of focal amplifications. *Nat. Commun.* **11**, 4374 (2020).

47. Suda, K. *et al.* Conversion from the 'oncogene addiction' to 'drug addiction' by intensive inhibition of the EGFR and MET in lung cancer with activating EGFR mutation. *Lung Cancer* (2012) doi:10.1016/j.lungcan.2011.11.007.

48.   Garnett, M. J., Rana, S., Paterson, H., Barford, D. & Marais, R. Wild-type and mutant B-RAF activate C-RAF through distinct mechanisms involving heterodimerization. *Mol. Cell* (2005) doi:10.1016/j.molcel.2005.10.022.

49.   Rushworth, L. K., Hindley, A. D., O'Neill, E. & Kolch, W. Regulation and Role of Raf-1/B-Raf Heterodimerization. *Mol. Cell. Biol.* (2006) doi:10.1128/mcb.26.6.2262-2272.2006.

50.   Montagut, C. *et al.* Elevated CRAF as a potential mechanism of acquired resistance to BRAF inhibition in melanoma. *Cancer Res.* (2008) doi:10.1158/0008-5472.CAN-07-6787.

51.   Alt, F. W., Kellems, R. E., Bertino, J. R. & Schimke, R. T. Selective multiplication of dihydrofolate reductase genes in methotrexate-resistant variants of cultured murine cells. *J. Biol. Chem.* **253**, 1357–1370 (1978).

52.   Nunberg, J. H., Kaufman, R. J., Schimke, R. T., Urlaub, G. & Chasin, L. A. Amplified dihydrofolate reductase genes are localized to a homogeneously staining region of a single chromosome in a methotrexate-resistant Chinese hamster ovary cell line. *Proc. Natl. Acad. Sci. U. S. A.* (1978) doi:10.1073/pnas.75.11.5553.

53.   Biedler, J. L., Melera, P. W. & Spengler, B. A. Specifically altered metaphase chromosomes in antifolate-resistant Chinese hamster cells that overproduce dihydrofolate reductase. *Cancer Genet. Cytogenet.* (1980) doi:10.1016/0165-4608(80)90079-5.

54.   McVey, M. & Lee, S. E. MMEJ repair of double-strand breaks (director's cut): deleted sequences and alternative endings. *Trends in Genetics* (2008) doi:10.1016/j.tig.2008.08.007.

55.   Klempner, S. J. *et al.* Identification of BRAF kinase domain duplications across multiple

tumor types and response to RAF inhibitor therapy. *JAMA Oncol.* (2016) doi:10.1001/jamaoncol.2015.4437.

56. Eleveld, T. F. *et al.* Relapsed neuroblastomas show frequent RAS-MAPK pathway mutations. *Nat. Genet.* **47**, 864–871 (2015).

57. Bhang, H. E. C. *et al.* Studying clonal dynamics in response to cancer therapy using high-complexity barcoding. *Nat. Med.* (2015) doi:10.1038/nm.3841.

58. Llabani, E. *et al.* Diverse compounds from pleuromutilin lead to a thioredoxin inhibitor and inducer of ferroptosis. *Nat. Chem.* (2019) doi:10.1038/s41557-019-0261-6.

59. Müller, J. *et al.* Low MITF/AXL ratio predicts early resistance to multiple targeted drugs in melanoma. *Nat. Commun.* (2014) doi:10.1038/ncomms6712.

60. Ghandi, M. *et al.* Next-generation characterization of the Cancer Cell Line Encyclopedia. *Nature* (2019) doi:10.1038/s41586-019-1186-3.

61. Consortium, E. P. *et al.* An integrated encyclopedia of DNA elements in the human genome. *Nature* (2013).

62. Gerosa, L. *et al.* Receptor-Driven ERK Pulses Reconfigure MAPK Signaling and Enable Persistence of Drug-Adapted BRAF-Mutant Melanoma Cells. *Cell Syst.* (2020) doi:10.1016/j.cels.2020.10.002.

63. Song, C. *et al.* Recurrent tumor cell–intrinsic and –extrinsic alterations during mapki-induced melanoma regression and early adaptation. *Cancer Discov.* (2017) doi:10.1158/2159-8290.CD-17-0401.

64. Barbie, D. A. *et al.* Systematic RNA interference reveals that oncogenic KRAS-driven cancers require TBK1. *Nature* (2009) doi:10.1038/nature08460.

65. Haq, R. *et al.* Oncogenic BRAF regulates oxidative metabolism via PGC1α and MITF.

Cancer Cell (2013) doi:10.1016/j.ccr.2013.02.003.

66. Cesi, G., Walbrecq, G., Zimmer, A., Kreis, S. & Haan, C. ROS production induced by BRAF inhibitor treatment rewires metabolic processes affecting cell growth of melanoma cells. *Mol. Cancer* (2017) doi:10.1186/s12943-017-0667-y.

67. Trotta, A. P. *et al.* Disruption of mitochondrial electron transport chain function potentiates the pro-apoptotic effects of MAPK inhibition. *J. Biol. Chem.* (2017) doi:10.1074/jbc.M117.786442.

68. Schöckel, L. *et al.* Targeting mitochondrial complex I using BAY 87-2243 reduces melanoma tumor growth. *Cancer Metab.* (2015) doi:10.1186/s40170-015-0138-0.

69. Vazquez, F. *et al.* PGC1α Expression Defines a Subset of Human Melanoma Tumors with Increased Mitochondrial Capacity and Resistance to Oxidative Stress. *Cancer Cell* (2013) doi:10.1016/j.ccr.2012.11.020.

70. Shen, S. *et al.* Melanoma Persister Cells Are Tolerant to BRAF/MEK Inhibitors via ACOX1-Mediated Fatty Acid Oxidation. *Cell Rep.* (2020) doi:10.1016/j.celrep.2020.108421.

71. Del Rey, M. Q. & Mancias, J. D. NCOA4-mediated ferritinophagy: A potential link to neurodegeneration. *Frontiers in Neuroscience* (2019) doi:10.3389/fnins.2019.00238.

72. Gao, M. *et al.* Ferroptosis is an autophagic cell death process. *Cell Res.* (2016) doi:10.1038/cr.2016.95.

73. Xu, K. *et al.* Structure and evolution of double minutes in diagnosis and relapse brain tumors. *Acta Neuropathol.* **137**, 123–137 (2019).

74. Vandevanter, D. R., Piaskowski, V. D., Casper, J. T., Douglass, E. C. & Von Hoff, D. D. Ability of circular extrachromosomal DNA molecules to carry amplified MYCN

protooncogenes in human neuroblastomas in vivo. *J. Natl. Cancer Inst.* (1990) doi:10.1093/jnci/82.23.1815.

75.   Nathanson, D. A. *et al.* Targeted therapy resistance mediated by dynamic regulation of extrachromosomal mutant EGFR DNA. *Science (80-.).* (2014) doi:10.1126/science.1241328.

76.   Akbani, R. *et al.* Genomic Classification of Cutaneous Melanoma. *Cell* (2015) doi:10.1016/j.cell.2015.05.044.

77.   Storlazzi, C. T. *et al.* Gene amplification as double minutes or homogeneously staining regions in solid tumors: origin and structure. *Genome Res.* **20**, 1198–206 (2010).

78.   Decarvalho, A. C. *et al.* Discordant inheritance of chromosomal and extrachromosomal DNA elements contributes to dynamic disease evolution in glioblastoma. *Nat. Genet.* **50**, 708–717 (2018).

79.   Shimizu, N., Shimura, T. & Tanaka, T. Selective elimination of acentric double minutes from cancer cells through the extrusion of micronuclei. *Mutat. Res. Mol. Mech. Mutagen.* **448**, 81–90 (2000).

80.   Gallant, J. N. *et al.* EGFR kinase domain duplication (EGFR -KDD) is a novel oncogenic driver in lung cancer that is clinically responsive to afatinib. *Cancer Discov.* (2015) doi:10.1158/2159-8290.CD-15-0654.

81.   Fenstermaker, R. A., Ciesielski, M. J. & Castiglia, G. J. Tandem duplication of the epidermal growth factor receptor tyrosine kinase and calcium internalization domains in A-172 glioma cells. *Oncogene* (1998) doi:10.1038/sj.onc.1202156.

82.   Frederick, L., Wang, X. Y., Eley, G. & James, C. D. Diversity and frequency of epidermal growth factor receptor mutations in human glioblastomas. *Cancer Res.* (2000).

83. Zhang, J. *et al.* Whole-genome sequencing identifies genetic alterations in pediatric low-grade gliomas. *Nat. Genet.* (2013) doi:10.1038/ng.2611.

84. Corazao-Rozas, P. *et al.* Mitochondrial oxidative phosphorylation controls cancer cell's life and death decisions upon exposure to MAPK inhibitors. *Oncotarget* (2016) doi:10.18632/oncotarget.7790.

85. Gopal, Y. N. V. *et al.* Inhibition of mTORC1/2 overcomes resistance to MAPK pathway inhibitors mediated by PGC1α and oxidative phosphorylation in melanoma. *Cancer Res.* (2014) doi:10.1158/0008-5472.CAN-14-1392.

86. Schieber, M. & Chandel, N. S. ROS function in redox signaling and oxidative stress. *Current Biology* (2014) doi:10.1016/j.cub.2014.03.034.

87. Yuan, L. *et al.* Braf mutant melanoma adjusts to BRAF/MEK inhibitors via dependence on increased antioxidant SOD2 and increased reactive oxygen species levels. *Cancers (Basel).* (2020) doi:10.3390/cancers12061661.

88. Rahal, A. *et al.* Oxidative stress, prooxidants, and antioxidants: The interplay. *BioMed Research International* (2014) doi:10.1155/2014/761264.

89. Dixon, S. J. *et al.* Ferroptosis: An iron-dependent form of nonapoptotic cell death. *Cell* (2012) doi:10.1016/j.cell.2012.03.042.

90. Hauck, A. K. & Bernlohr, D. A. Oxidative stress and lipotoxicity. *J. Lipid Res.* (2016) doi:10.1194/jlr.r066597.

91. Yang, W. S. *et al.* Regulation of ferroptotic cancer cell death by GPX4. *Cell* (2014) doi:10.1016/j.cell.2013.12.010.

92. Hou, W. *et al.* Autophagy promotes ferroptosis by degradation of ferritin. *Autophagy* (2016) doi:10.1080/15548627.2016.1187366.

93.   Wang, L. *et al.* An Acquired Vulnerability of Drug-Resistant Melanoma with Therapeutic Potential. *Cell* (2018) doi:10.1016/j.cell.2018.04.012.

94.   Søndergaard, J. N. *et al.* Differential sensitivity of melanoma cell lines with BRAFV600Emutation to the specific Raf inhibitor PLX4032. *J. Transl. Med.* (2010) doi:10.1186/1479-5876-8-39.

95.   Hong, A. *et al.* Exploiting drug addiction mechanisms to select against mapki-resistant melanoma. *Cancer Discov.* (2018) doi:10.1158/2159-8290.CD-17-0682.

96.   Kim, D. K. Estimating doubling time of cells in vitro. *In Vitro Cellular & Developmental Biology - Animal: Journal of the Society for In Vitro Biology* (1995) doi:10.1007/BF02634250.

97.   Rajkumar, U. *et al.* EcSeg: Semantic Segmentation of Metaphase Images Containing Extrachromosomal DNA. *iScience* (2019) doi:10.1016/j.isci.2019.10.035.

98.   Robinson, J. T. *et al.* Integrative genomics viewer. *Nature Biotechnology* (2011) doi:10.1038/nbt.1754.

99.   Garvin, T. *et al.* Interactive analysis and assessment of single-cell copy-number variations. *Nature Methods* (2015) doi:10.1038/nmeth.3578.

100. Langmead, B. Alignment with Bowtie. *Curr Protoc Bioinforma.* (2011) doi:10.1002/0471250953.bi1107s32.Aligning.

101. Li, H. [Heng Li - Compares BWA to other long read aligners like CUSHAW2] Aligning sequence reads, clone sequences and assembly contigs with BWA-MEM. *arXiv Prepr. arXiv* (2013).

102. der Auwera, G. A. *Genomics in the cloud : using Docker, GATK, and WDL in Terra. Genomics in the cloud : using Docker, GATK, and WDL in Terra* (2020).

103.   Talevich, E., Shain, A. H., Botton, T. & Bastian, B. C. CNVkit: Genome-Wide Copy
       Number Detection and Visualization from Targeted DNA Sequencing. *PLoS Comput.*
       Biol. (2016) doi:10.1371/journal.pcbi.1004873.

104.   Deshpande, V. *et al.* Exploring the landscape of focal amplifications in cancer using
       AmpliconArchitect. *Nat. Commun.* (2019) doi:10.1038/s41467-018-08200-y.

105.   Wala, J. A. *et al.* SvABA: Genome-wide detection of structural variants and indels by
       local assembly. *Genome Res.* (2018) doi:10.1101/gr.221028.117.

106.   Raeisi Dehkordi, S., Luebeck, J. & Bafna, V. FaNDOM: Fast nested distance-based
       seeding of optical maps. *Patterns* (2021) doi:10.1016/j.patter.2021.100248.

107.   Burgin, J., Molitor, C. & Mohareb, F. MapOptics: A light-weight, cross-platform
       visualization tool for optical mapping alignment. *Bioinformatics* (2019)
       doi:10.1093/bioinformatics/bty1013.

108.   Dobin, A. *et al.* STAR: Ultrafast universal RNA-seq aligner. *Bioinformatics* (2013)
       doi:10.1093/bioinformatics/bts635.

109.   Vivian, J. *et al.* Toil enables reproducible, open source, big biomedical data analyses.
       Nature Biotechnology (2017) doi:10.1038/nbt.3772.

110.   Van der Auwera, G. A. *et al.* From fastQ data to high-confidence variant calls: The
       genome analysis toolkit best practices pipeline. *Curr. Protoc. Bioinforma.* (2013)
       doi:10.1002/0471250953.bi1110s43.

111.   Gu, Z., Eils, R. & Schlesner, M. Complex heatmaps reveal patterns and correlations in
       multidimensional genomic data. *Bioinformatics* (2016)
       doi:10.1093/bioinformatics/btw313.

112.   Wang, V. E. *et al.* Adaptive Resistance to Dual BRAF/MEK Inhibition in BRAF-Driven

Tumors through Autocrine FGFR Pathway Activation. *Clin. Cancer Res.* (2019) doi:10.1158/1078-0432.CCR-18-2779.

113. Kemper, K. *et al.* Intra- and inter-tumor heterogeneity in a vemurafenib-resistant melanoma patient and derived xenografts. *EMBO Mol. Med.* (2015) doi:10.15252/emmm.201404914.

114. Long, G. V. *et al.* Increased MAPK reactivation in early resistance to dabrafenib/trametinib combination therapy of BRAF-mutant metastatic melanoma. *Nat. Commun.* (2014) doi:10.1038/ncomms6694.

115. Shen, C. H. *et al.* Loss of cohesin complex components STAG2 or STAG3 confers resistance to BRAF inhibition in melanoma. *Nat. Med.* (2016) doi:10.1038/nm.4155.

116. Van Allen, E. M. *et al.* The genetic landscape of clinical resistance to RAF inhibition in metastatic melanoma. *Cancer Discov.* (2014) doi:10.1158/2159-8290.cd-13-0617.

117. Villanueva, J. *et al.* Concurrent MEK2 Mutation and BRAF Amplification Confer Resistance to BRAF and MEK Inhibitors in Melanoma. *Cell Rep.* (2013) doi:10.1016/j.celrep.2013.08.023.

118. Ritz, C., Baty, F., Streibig, J. C. & Gerhard, D. Dose-response analysis using R. *PLoS One* (2015) doi:10.1371/journal.pone.0146021.

119. Li, B. & Dewey, C. N. RSEM: Accurate transcript quantification from RNA-Seq data with or without a reference genome. *BMC Bioinformatics* (2011) doi:10.1186/1471-2105-12-323.

120. Hänzelmann, S., Castelo, R. & Guinney, J. GSVA: Gene set variation analysis for microarray and RNA-Seq data. *BMC Bioinformatics* (2013) doi:10.1186/1471-2105-14-7.

121. Liberzon, A. *et al.* The Molecular Signatures Database Hallmark Gene Set Collection.

Cell Syst. (2015) doi:10.1016/j.cels.2015.12.004.

122. Subramanian, A. *et al.* Gene set enrichment analysis: A knowledge-based approach for interpreting genome-wide expression profiles. *Proc. Natl. Acad. Sci.* **102**, 15545–15550 (2005).